

# On The Development of Multidimensional Progenitor Models For Core-collapse Supernovae

C. E. FIELDS<sup>1,2,3,4,\*</sup> AND SEAN M. COUCH<sup>1,4,5,3</sup>

<sup>1</sup>*Department of Physics and Astronomy, Michigan State University, East Lansing, MI 48824, USA*

<sup>2</sup>*Center for Theoretical Astrophysics, Los Alamos National Lab, Los Alamos, NM 87545, USA*

<sup>3</sup>*Joint Institute for Nuclear Astrophysics - Center for the Evolution of the Elements, USA*

<sup>4</sup>*Department of Computational Mathematics, Science, and Engineering, Michigan State University, East Lansing, MI 48824, USA*

<sup>5</sup>*National Superconducting Cyclotron Laboratory, Michigan State University, East Lansing, MI 48824, USA*

## ABSTRACT

Multidimensional hydrodynamic simulations of shell convection in massive stars suggest the development of aspherical perturbations that may be amplified during iron core-collapse. These perturbations have a crucial and qualitative impact on the delayed neutrino-driven core-collapse supernova explosion mechanism by increasing the total stress behind the stalled shock. In this paper, we investigate the properties of a  $15 M_{\odot}$  model evolved in 1-, 2-, and 3-dimensions (3D) for the final  $\sim 424$  seconds before gravitational instability and iron core-collapse using MESA and the FLASH simulation framework. We find that just before collapse, our initially perturbed fully 3D model reaches angle-averaged convective velocity magnitudes of  $\approx 240\text{--}260 \text{ km s}^{-1}$  in the Si- and O-shell regions with a Mach number  $\approx 0.06$ . We find the bulk of the power in the O-shell resides at large scales, characterized by spherical harmonic orders ( $\ell$ ) of 2-4, while the Si-shell shows broad spectra on smaller scales of  $\ell \approx 30\text{--}40$ . Both convective regions show an increase in power at  $\ell = 5$  near collapse. We show that the 1D MESA model agrees with the convective velocity profile and speeds of the Si-shell when compared to our highest resolution 3D model. However, in the O-shell region, we find that MESA predicts speeds approximately *four* times slower than all of our 3D models suggest. All eight of the multi-dimensional stellar models considered in this work are publicly available.

*Keywords:* convection — hydrodynamics — stars: evolution — stars: interiors — supernovae: general

## 1. INTRODUCTION

Stars with an initial zero age main-sequence (ZAMS) mass of greater than approximately  $8\text{--}10 M_{\odot}$  may end their lives via core-collapse supernova (CCSN) explosions (Janka 2012; Farmer et al. 2015; Woosley & Heger 2015; Woosley et al. 2002). Core-collapse supernova explosions facilitate the evolution of chemical elements throughout galaxies (Timmes et al. 1995; Pignatari et al. 2016; Côté et al. 2017), produce stellar mass compact object systems (Özel et al. 2012; Sukhbold et al. 2016; Couch et al. 2019), and provide critical feedback to galaxy and star formation (Hopkins et al. 2011; Botticella et al. 2012; Su et al. 2018). Hydrodynamic simulations of CCSNe have helped inform our understanding of all

of these aspects, beyond that which can be inferred directly from current observations.

CCSN simulations now include 3D hydrodynamics as well as more accurate treatments of key physical aspects of the problem. Many advances have been made to produce such simulations, such as the inclusion of two-moment neutrino transport schemes (e.g., Hanke et al. 2013; Lentz et al. 2015; O’Connor & Couch 2018a; Glas et al. 2019; Vartanyan et al. 2019), a general relativistic treatment for gravity as opposed to a Newtonian approach (Roberts et al. 2016; Müller et al. 2017), and spatial resolutions that allow us to accurately capture the Reynolds stress (Radice et al. 2016; Nagakura et al. 2019), a key component in the dynamics of the shock. Despite these advances, the vast majority of these simulations rely on one dimensional (1D) initial conditions for the progenitor star. These progenitors are typically produced using stellar evolution codes where convection is treated using mixing length theory (MLT) (Böhm-Vitense 1958; Cox & Giuli 1968). MLT has been shown to accurately represent convection in 1D models when calibrated to radiation hydrodynamic

Corresponding author: C. E. Fields  
fieldsc9@msu.edu

\* NSF Graduate Research Fellow  
Ford Foundation Predoctoral Fellow

simulations of surface convection in the Sun (Trampedach et al. 2014). Despite the utility of MLT in 1D stellar models, multidimensional effects in the late stages of nuclear burning in the life of a massive star can lead to initial conditions that differ significantly from what 1D stellar evolution models suggest (Arnett et al. 2009; Arnett & Meakin 2011; Viallet et al. 2013).

Couch & Ott (2013) investigated the impact of asphericity in the progenitor star on the explosion of a  $15 M_{\odot}$  stellar model that has been investigated in detail (Woosley & Heger 2007). Motivated by results of multidimensional shell burning in massive stars (Meakin & Arnett 2007; Arnett & Meakin 2011), they implemented velocity perturbations within the Si-shell to assess the impact on the explosion dynamics. They found that the models with the velocity perturbations either exploded successfully or evolved closer to explosion where the models without the perturbations failed to successfully revive the stalled shock. The non-radial velocity perturbations resulted in stronger convection and turbulence in the gain layer. These motions play a significant role in contributing to the turbulent pressure and dissipation which can supplement the thermal pressure behind the shock and, thus, enable explosions at lower effective neutrino heating rates (Couch & Ott 2015; Mabanta & Murphy 2018). Couch & Ott (2013) compared models with and without perturbations and with either fiducial or slightly enhanced neutrino heating. Their 3D model *without* initial perturbations but slightly enhanced heating (2% larger than fiducial) followed a similar trajectory as the perturbed model (peak perturbation Mach number of  $\mathcal{M}_{\text{pert}} = 0.2$ ) with no enhanced heating. However, neither of these models were able to revive the stalled shock and both resulted in a failed explosion. These results suggested that the multidimensional structure of the progenitor star can provide a favorable impact on the likelihood for explosion by increasing the total stress, both thermal and turbulent, behind the shock. Without perturbations, the progenitor star used by Couch & Ott (2013) required more neutrino heating (5% larger than fiducial) to achieve shock revival (Couch & O’Connor 2014).

One of the first efforts to produce multidimensional CCSN progenitors began with the seminal work of Arnett (1994). They performed hydrodynamic O-shell burning simulations in a two-dimensional wedge using an approximate 12 species network. In this work, they found maximum flow speeds that approached  $\approx 200 \text{ km s}^{-1}$  which induced density perturbations and also observed mixing beyond stable boundaries. Much later, Meakin & Arnett (2007) presented the first results of O-shell burning in 3D. They evolved a 3D wedge encompassing the O-shell burning region using the PROMPT code for a total of about eight turnover timescales. In comparing the 3D model to a similar 2D model they found flow speeds in the 2D model were significantly larger and also

found that the interaction between the convectively stable layers with large convective plums can facilitate the generation of waves. The combined efforts of these previous works all suggested the need for further investigation into the role of the late time properties of CCSN progenitors near collapse.

Building upon previous work, Couch et al. (2015) (hereafter C15) presented the first three-dimensional (3D) simulation of iron core collapse in a  $15 M_{\odot}$  star. They evolved the model in 3D assuming octant symmetry and an approximate 21 isotope network for a total of  $\approx 160$  s up to the point of gravitational instability and iron core collapse. Their simulation captured  $\sim 8$  convective turnovers in the Si-burning shell region with speeds in the Si-shell region on the order of several hundred  $\text{km s}^{-1}$  and significant non-radial kinetic energy. They then followed the 3D progenitor model through core collapse and bounce to explosion using similar methods as in Couch & O’Connor (2014), i.e. parameterized deleptonization, multispecies neutrino leakage scheme, and Newtonian gravity. When comparing the explosion of the 3D progenitor model to the angle-average of the same model, they find that the turbulent kinetic energy spectrum ahead of the shock front (in the accretion flow) was more than an order-of-magnitude larger for the 3D case during accretion of the Si-shell, around post-bounce times of  $t_{\text{pb}} = 125 \pm 25$  ms. The more turbulent accretion flow led to enhanced total turbulent kinetic energy in the gain region by up to almost a factor of two for the 3D initial conditions than the angle-averaged model, with most of the turbulent kinetic energy residing at scales of  $\ell \approx 6 - 10$ , where  $\ell$  is the principle spherical harmonic order. These differences resulted in an overall more rapidly expanding shock radius and a diagnostic explosion energy approximately a factor of two larger than the 1D initial model. However, the model presented in that work suffered from approximations that may have affected the results. The main issues were the use of octant symmetry and the modification of the electron capture rates used in the simulation. The first of these approximations can lead to a suppression of perturbations of very large scales while the second can lead to larger convective speeds within the Si-shell region due to the rapid artificial contraction of the iron core.

Müller et al. (2016) aimed to address these issues by conducting a full  $4\pi$  3D simulation of O-shell burning in a  $18 M_{\odot}$  progenitor star. Using the Prometheus hydrodynamics code they evolved the model in 3D for  $\sim 294$  s up to the point of iron core collapse. They alleviate the use of enhanced electron capture rates by imposing an inner boundary condition that follows the radial trajectory of the outer edge of the Si-shell according to the 1D initial model generated by the Kepler stellar evolution code. In their simulation, they capture approximately 9 turnover timescales in the O-shell finding Mach numbers that reach values of  $\sim 0.1$  as well as a large scale  $l = 2$  mode that emerges near the point of col-

lapse. Their results build on those of C15 with further evidence suggesting the need for full  $4\pi$  simulations. Recently, (Yadav et al. 2020) presented a  $4\pi$  3D simulation of O-shell burning where a violent merging of the O/Si interface and Ne layer merged prior to gravitational collapse. This simulation of an  $18.88 M_{\odot}$  progenitor for 7 minutes captured the mixing that occurred after the merging and was found to lead to Mach numbers of  $\sim 0.13$  near collapse. All of these efforts suggest that 3D progenitor structure increases the likelihood for explosion of massive stars by the delayed neutrino heating mechanism.

In this paper, we present 1D, 2D, and 3D hydrodynamical simulations of Si- and O- shell burning of a  $15 M_{\odot}$  progenitor star for the final  $\sim 424$  seconds of its life up to the point of gravitational instability and iron core collapse. Using these models, we: 1) provide a detailed description of the convective regions in the Si- and O- burning shells, 2) estimate key stellar evolution parameters that may impact the explosion properties of CCSNe and compare them to their 1D counterparts, and 3) study how the properties of these models may depend on resolution, dimensionality/symmetry, and initial perturbations. In order to self-consistently simulate secular core contraction and ultimate collapse, we include the iron core and both Si- and O-shell regions in our simulation. To address the dependence of resolution, dimensionality, and symmetry on our results we consider 2D and 3D models at varying finest resolution and cylindrical versus octant symmetry, respectively. We improve on the work of C15 by alleviating the use of accelerated electron capture rates, evolving two 3D simulations that cover the full solid angle ( $4\pi$  steradian) rather than octant symmetry, and significantly increase the timescale of the simulation. Lastly, to assess the impact of initial conditions, our two  $4\pi$  3D models differ only in the initialization of the velocity field. Using these models, we characterize the qualitative properties of the flow amongst different parameter choices while also comparing to the predicted properties of the 1D input model for our simulations. We present a detailed analysis of the convective properties of the  $4\pi$  3D models and discuss the implications for the 3D state of CCSN progenitors at collapse. This paper is organized as follows. In Section 2 we discuss our computational methods and input physics, in Section 3 we present the results of our 2- and 3D hydrodynamical FLASH simulations, Section 4 summarizes our results and compares them to previous efforts.

## 2. METHODS AND COMPUTATIONAL SETUP

Our methods follow closely those used in C15 in that we evolve a 1D spherically symmetric stellar evolution model using MESA and, at a point near iron core collapse, map the model into the FLASH simulation framework and continue

the evolution in multi-D to collapse. In the following subsections, we will describe these steps in detail.

### 2.1. 1D MESA Stellar Evolution Model

We evolve a  $15 M_{\odot}$  solar metallicity stellar model using the open-source stellar evolution toolkit, Modules for Experiments in Stellar Astrophysics (MESA) (Paxton et al. 2011, 2013, 2015, 2018, 2019). The model is evolved from the pre-main sequence to a time approximately 424 seconds before iron core collapse, defined by MESA as the time when any location of the iron core reaches an infall velocity of greater than  $1000 \text{ km s}^{-1}$ . We use temporal and spatial parameters similar to those used in Farmer et al. (2016) and Fields et al. (2018). These parameters result in timesteps on the order of  $\bar{\delta}t \approx 41 \text{ kyr}$  during the main sequence,  $\bar{\delta}t \approx 24 \text{ yr}$  during core carbon burning, and  $\bar{\delta}t \approx 19 \text{ sec}$  when the model is stopped. At the point when the model is stopped, the model has 3611 cells with an enforced maximum  $\bar{\delta}m \approx 0.01 M_{\odot}$ . The MESA model uses an  $\alpha$ -chain network that follows 21 isotopes from  $^1\text{H}$  to  $^{56}\text{Cr}$ . This network is chosen for its computational efficiency and to match the network currently implemented in FLASH and used in (Couch et al. 2015). This approximate network aims to capture important aspects of pre-supernova evolution of massive star models which include reactions between heavy ions and iron-group photodisintegration and similar approaches have been used in many previous studies (Heger et al. 2000; Heger & Woosley 2010). We include mass loss using the ‘Dutch’ wind scheme with an efficiency value of 0.8. Mixing processes due to convective overshoot, thermohaline, and semi-convection are considered with values from Fields et al. (2018). We do not include rotation and magnetic fields in this model.

In Figure 1 we show the specific entropy, electron fraction, and mass density profiles as a function of mass coordinate from the MESA model at the point which it is mapped into FLASH. The dashed black line denotes the edge of the domain considered in the FLASH simulations. Overall, the model used in this work has a similar structure to the progenitor used in C15 except for the case of the lower central electron fraction in the core. This difference is partially due to the different network used in C15, a basic 8 isotope network that was automatically extended during evolution compared to our static 21 isotope network used in the MESA model for this work. The input MESA model in C15 also had a slightly smaller initial iron core mass,  $1.3 M_{\odot}$ , than the model considered here.

Figure 2 shows the mass fraction profiles for some of the most abundant isotopes for the input MESA model. The label ‘Iron’ denotes the sum of mass fractions of  $^{52,54,56}\text{Fe}$  isotopes. At the point of mapping the stellar model has an iron core mass of approximately  $1.44 M_{\odot}$ . The Si-shell region is located at a specific mass coordinate of  $m \approx 1.53 - 1.68 M_{\odot}$

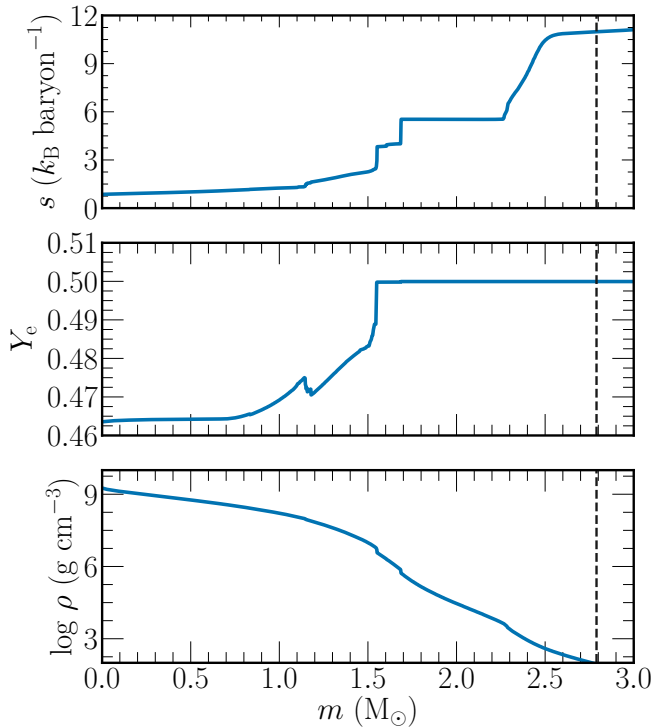


**Figure 1.** Specific entropy, electron fraction, and mass density profiles as function of stellar mass for the 1D MESA model at the time of mapping into FLASH. The dashed black vertical line denotes the edge of the domain used in the FLASH simulations.

while the O-shell region extends from the edge of the Si-shell out to mass coordinate of  $m \approx 2.26 M_{\odot}$ . Figure 3 shows the time evolution of the Brunt-Väisälä frequency (left) and convective velocity speeds (right) as a function of mass coordinate as predicted by MESA for the 1D model evolved from the point at which it is mapped into FLASH until core collapse. The 1D model predicts convective speeds in the O-shell regions with a peak of approximately  $100 \text{ km s}^{-1}$  up to the point of collapse. In the Si-shell region, only the inner most region is convectively active with speeds on the order of those in the O-shell. At a time of  $t \approx 200 \text{ s}$ , the innermost Si-shell burning convective region ceases and convective proceeds instead at a further mass coordinate of  $m \approx 1.60 - 1.68 M_{\odot}$  with speeds increasing to values greater than in the O-shell near collapse at  $\approx 160 \text{ km s}^{-1}$ .

## 2.2. 2- and 3D FLASH Stellar Evolution Model

### 2.2.1. Overview

We perform a total of eight multidimensional stellar evolution models at various resolutions and symmetries. All models are evolved using the FLASH simulation framework (Fryxell et al. 2000; Dubey et al. 2009). Similar to Couch et al. (2015), we utilize the “Helmholtz” EoS (Timmes & Swesty 2000) and the same 21 isotope network but with an

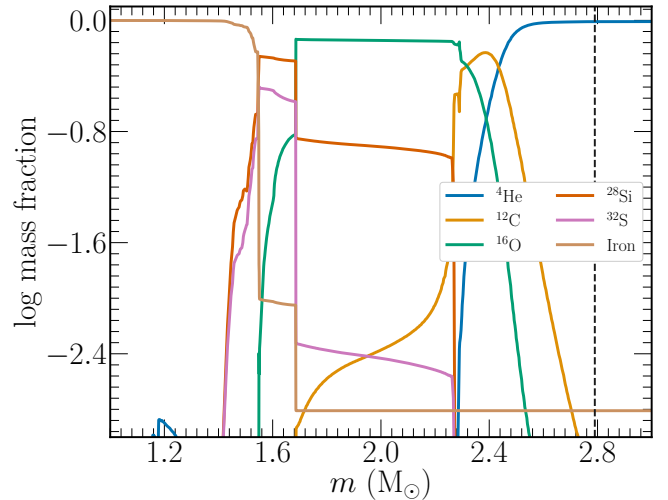


**Figure 2.** Mass fractions of the most abundant isotopes as a function of stellar mass for the 1D MESA model at time of mapping into FLASH. The label ‘Iron’ denotes the sum of mass fractions of  $^{52,54,56}\text{Fe}$  isotopes. The dashed black vertical line denotes the edge of the domain in FLASH.

improvement to the weak reaction rate used for electron capture onto  $^{56}\text{Ni}$ . The original network used tabulated rates from Mazurek et al. (1974) while the updated rates were adopted from Langanke & Martínez-Pinedo (2000). The new rates are enhanced by close to a factor of 5-10 alleviating any need to artificially enhance the total electron capture rates in the models presented in this work and are also in agreement with the table values used in MESA.

### 2.2.2. Hydrodynamics, Gravity, and Domain

The equations of compressible hydrodynamics are solved using FLASH’s directionally unsplit piecewise parabolic method (PPM) (Lee & Deane 2009) and HLLC Riemann solvers (Toro 1999) with a Courant factor of 0.8. Self-gravity is solved assuming a spherically symmetric (monopole) gravitational potential approximation (Couch et al. 2013). Our computational domain extends to  $10^{10} \text{ cm}$  from the origin in each dimension for both the 2D and 3D models. Four 2D models are evolved with varying levels of finest grid spacing resolution of 8, 16, 24, and 32 km. The 2D models use cylindrical geometry with symmetry about the azimuthal direction. Four 3D models are evolved: two assuming octant symmetry with two different values of finest grid resolution, 16 and 32 km, and two full  $4\pi$  3D models at 32 km finest grid resolution, one with an initialized velocity field and one without. All 3D models use Cartesian coordinates. The models are labeled according to their dimensionality and finest grid spacing, and in the case of 3D according to the use of octant symmetry or not. For example, the 3D 32 km octant model is labelled 3DOct32km for ease of model identi-

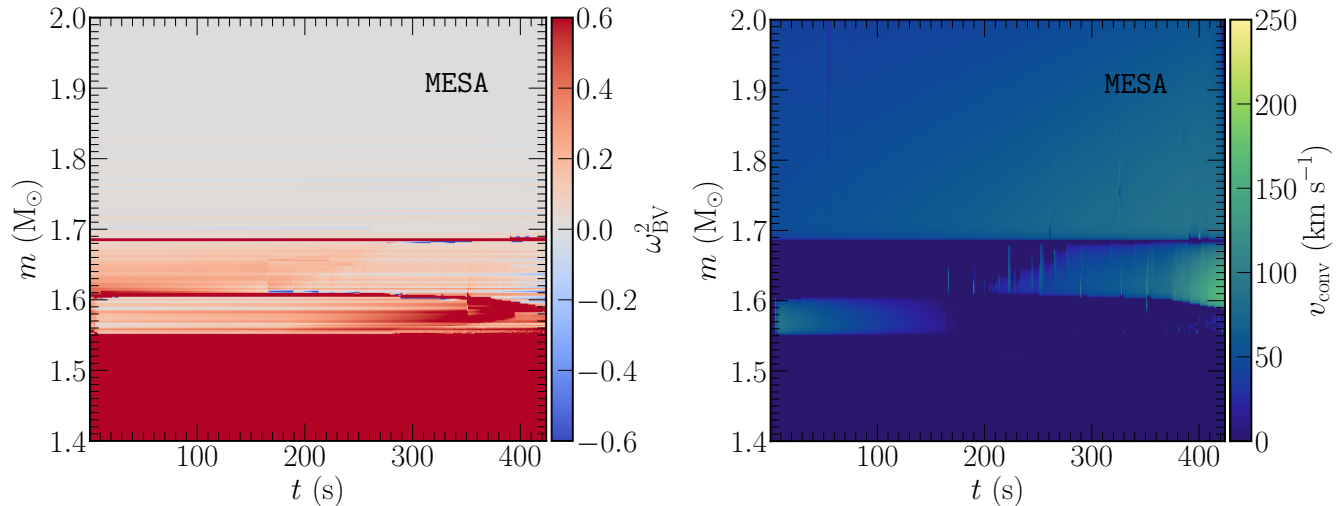


**Figure 3.** Time evolution of the 1D profile data for the MESA model. The (left) subplot shows the Brunt-Väisälä frequency while the (right) shows the convective velocity speeds according to MLT. The red regions denote regions that are stable against convection while gray and blue regions show regions that are unstable to convection according to MESA.

cation throughout the remainder of this paper. The initially perturbed  $4\pi$  3D model is labeled 3D32kmPert.

The velocity field initialization for the perturbed model follows the methods used in Muller & Janka (2015) and extended to 3D in O’Connor & Couch (2018b). The method introduces solenoidal velocity perturbations to the  $v_r$  and  $v_\theta$  components using spherical harmonics and sinusoidal radial dependence. We use the convective velocity profile of the 1D MESA model at the time of mapping to inform our choices of parameters to initialize the velocity field. We take the innermost convective Si-shell region to be from  $r_{1,\min} \approx 2220$  km to  $r_{1,\max} \approx 2740$  km, and choose spherical harmonic coefficients to be  $\ell = 5, m = 1$  with a single radial sinusoid ( $n = 1$ ). The second convective Si-shell region, at  $r_{2,\min} \approx 2740$  km to  $r_{2,\max} \approx 3760$  km, uses the same spherical harmonic and radial numbers as the first;  $n = 1, \ell = 5, m = 1$ . Lastly, the O-shell region, taken to be  $r_{3,\min} \approx 3770$  km to  $r_{3,\max} \approx 26,620$  km, assumes an initially larger scale flow with quantum numbers of  $n = 1, \ell = 5, m = 3$ .

All velocity amplitude scaling factors ( $C$ ) for the initial perturbations were chosen to match approximately 1% (in the Si-shell regions) and 5% (in the O-shell region) of the convective velocity speed as predicted by the MESA model at time of mapping. The resulting perturbations led to an angle-averaged Mach number of  $\mathcal{M} \approx 2 \times 10^{-3}$  and  $\mathcal{M} \approx 1.3 \times 10^{-2}$  in the Si-shell and O-shell regions, respectively. For comparison, the scaling factors used in (O’Connor & Couch 2018b) to replicate pre-collapse perturbations were on the order of  $\mathcal{O} \sim 10^3$  larger than values used here. In terms of the total initial kinetic energy the perturbed model begins with a value of  $E_{\text{kin.}} \approx 5.8 \times 10^{45}$  erg, approximately 4% of the peak total kinetic energy observed at later times.

All models utilize adaptive mesh refinement (AMR) with up to eight levels of refinement. To give an example of the grid structure for our models we consider the refinement boundaries for the 2D8km and 2D32km models. In both of these models, the entire Si-shell region has a grid resolution of 32 km with effective angular resolution of  $\approx 0.9^\circ$  to  $0.5^\circ$  at the base ( $\approx 2000$  km) and edge of the shell ( $\approx 3500$  km), respectively. The resolution within the Si-shell region for these model corresponds to an average of  $\approx 5\%$  of the local pressure scale height,  $H_p$ . The grid resolution in the 2D models are representative of the respective 3D models as well. The two finer resolution levels of the 2D8km model are situated within the iron core with the second highest level of refinement at the base of the Si-shell region and down to a radius of 1000 km. In this region, the 2D8km and 2D32km grid resolutions provide a value of  $\approx 6\%$  and  $\approx 12\%$  of  $H_p$ , respectively. The O-shell region in these models is at 64 km resolution out to a radius of  $\approx 6000$  km then decreases to 128 km from there to 10,000 km. Within these two regions the effective angular resolution ranges from  $0.73^\circ$  to  $0.61^\circ$  and corresponds to an average of  $\approx 0.04H_p$  and  $\approx 0.05H_p$ , respectively. In the 2D32km, the finest resolution level goes out to a radius of 3500 km, the approximate edge of the Si-shell, giving the model similar resolution in this and the O-shell to that of the 2D8km without the two finer resolution levels within the iron core. The location of refinement levels used is determined as a function of radius and chosen based on logarithmic changes in specific density, pressure, and velocity. The refinement levels are static throughout the simulation and chosen based on the input model.

For the 3D octant symmetry planes and the 2D axis plane we use reflecting boundary conditions while the outer boundaries utilize a boundary condition that applies power-law ex-

trapolations of the velocity and density fields to approximate the roughly hydrostatic outer envelope of the stellar interior. The  $4\pi$  3D models use the same custom boundary condition at all domain edges. To help reduce any artificial transients that occur from mapping from a Lagrangian to an Eulerian code with different grid resolution, we use the approach of Zingale et al. (2002). This approach takes the initial 1D MESA model and maps it to a uniform grid with resolution four times finer than that used in our FLASH grid. The density in the remapped model is then slightly modified while the pressure is held fixed to force the model into hydrostatic equilibrium (HSE), such that it satisfies

$$\nabla P = \rho g, \quad (1)$$

in the absence of initial velocities. The procedure is then closed by calling the equation of state (EOS) for the new profile.

### 2.2.3. Nuclear Burning

During the growth of the iron core, thermal support is removed from the core due to photo-disintegration of iron nuclei that cause the gas to cool. The subsequent contraction of the stellar core causes an increase in the rate of electron captures onto protons therefore decreasing the pressure support contribution from electron degeneracy. This further reduction of pressure support in the core accelerates nuclear burning in the silicon burning shell leading to faster growth of the iron core. In the moments prior to iron core collapse the core moves towards nuclear statistical equilibrium while the neutrino cooling and photo-disintegration rates begin to dominate and lead to a negative specific nuclear energy generation rate,  $\epsilon_{\text{nuc}}$ , in the inner core. Within this cooled material, the electron capture rates increase significantly and give rise to a positive specific  $\epsilon_{\text{nuc}}$  and cause the temperature to rise again. Within this region a numerical instability can occur for calculations which employ operator split burning and hydrodynamics (Timmes et al. 2000). In order to avoid this instability from occurring in the models considered here, we place a limiter on the maximum timestep such that any change in the internal energy across all zones in the domain is limited to a maximum of a 1% per timestep.

The large and opposite specific nuclear energy generation rates within the core can also lead to significant difficulties in solving the nuclear reaction network at a given timestep and lead to significant load imbalance of the computational workload per MPI rank. Zones within the core can take several hundred iterations to obtain a solution while outside of the iron core, a solution is found in a fraction of the time. In order to help circumvent these issues, we employ a moving “inner boundary condition” within the iron core, well below the region of interest for this paper. For all simulations considered here, the profiles of  $\rho$ ,  $Y_e$ , and  $P$  in the inner 1000 km

of the models are evolved according to the profile from the MESA model at the corresponding time. A 2D table is constructed from the MESA profile data from the point of mapping to FLASH ( $\approx 424$  s) until iron core collapse. Four point Lagrange linear interpolation is then performed in time and radius to ensure accurate values are mapped for the FLASH models, which take on the order of 100 timesteps for every MESA timestep. This mapping effectively provides a time-dependent inner boundary condition that ensures the model follows the central evolution of the MESA model while still allowing us to capture the pertinent multi-D hydrodynamic behavior with FLASH.

For all models, we simulate  $\approx 424$  s of evolution prior to collapse capturing Si- and O-shell burning up to gravitational instability and iron core collapse. The full  $4\pi$  3D models had an approximate total of 46M zones, took  $\approx 0.6$  M core hours on the laconia compute cluster at Michigan State University. All the multidimensional CCSN progenitor models considered in this work are available publicly at [10.5281/zenodo.3976246](https://doi.org/10.5281/zenodo.3976246).

## 3. MULTI-DIMENSIONAL EVOLUTION TO IRON CORE-COLLAPSE

### 3.1. Results from 2D Simulations

We evolve a total of four 2D simulations at 8, 16, 24, and 32 km finest grid spacing resolution. In the following subsection we consider the global properties of all of the 2D models, compare the lowest and highest resolution model, and consider in detail the convective properties of the highest resolution 2D model.

The structure of the flow at large scale within the shell burning regions can have a significant impact on the CCSN explosion mechanism. Perturbations within these region can be amplified during collapse of the iron core and aid in the development of turbulence during explosion (Lai & Goldreich 2000; Couch & Ott 2013, 2015). In Figure 4 we show slices of the magnitude of the velocity field for the  $2D_{32\text{km}}$  (left subplots) and  $2D_{8\text{km}}$  models (right subplots) at four different times. At early times, we see convection developing in a similar manner for both the 8 km and 32 km models. Both models exhibit a “square” like imprint in the velocity field that is due to the stiff entropy barrier at the edge of the Si-shell region interacting with the Cartesian-like 2D axisymmetric grid. We also observe high-velocity flows restricted to the vicinity of the axis of symmetry, an artifact commonly observed in 2D axisymmetric simulations. Around  $t = 200$  s both models become characterized by large scale cyclones in the O-shell region with convective speeds of  $\approx 100 - 120$  km  $\text{s}^{-1}$ , three to five times larger than in the Si-shell region. At late times, beyond  $t = 350$  s, the 8 km model appears to reach flow speeds in the Si-shell that are on the order of those observed in the O-shell. In the O-shell, the scale of the convec-

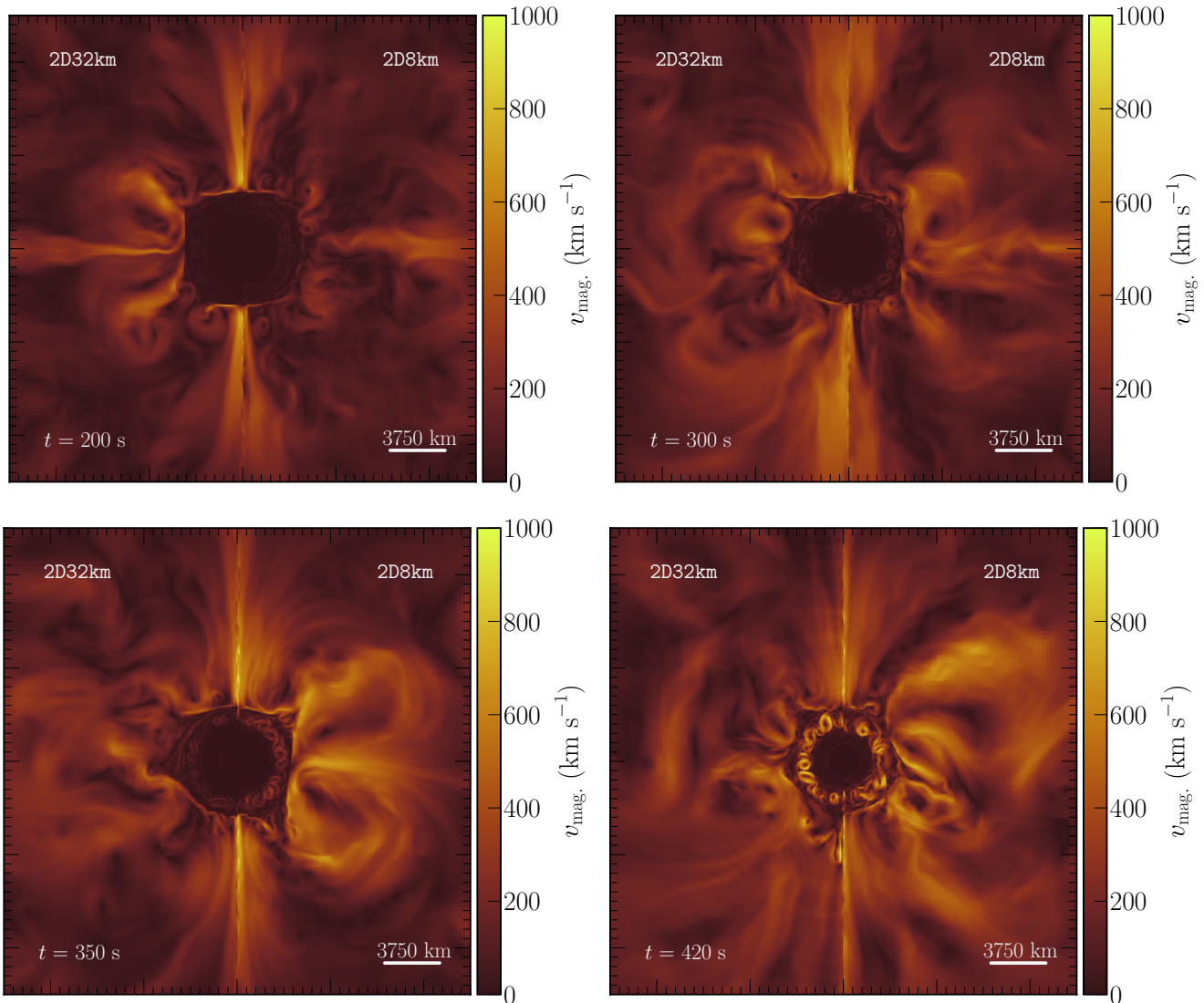


**Figure 4.** Slices of the the magnitude of the velocity field for the 2D32km (left) and 2D8km model (right) at four different times. At  $t = 200$  s, both models exhibit a “square” like imprint in the velocity field that is due to the stiff entropy barrier at the edge of the Si-shell along with increased velocity speeds along the axis. These speeds are due to numerical artifacts common in 2D simulations assuming axisymmetry. The increased velocity along the axis causes outflows in the positive radial direction at the top and bottom of the Si-shell region. Beyond  $t = 200$  s, both models become characterized by large scale cyclones in the O-shell region with convective activity in the Si-shell having three to five times slower flow speeds.

tion increases as cyclones on the order of  $\approx 4000$  km dominate the flow with the scale of convection within the Si-shell region being restricted by the width of the shell. Seconds prior to collapse, the 32 km model reaches Si-shell convective speeds that agree with the 8 km model.

To begin our assessment of the convective properties of the models, we compute the angle-averaged maximum Mach number, defined as,

$$\langle \mathcal{M} \rangle = \left\langle \frac{|\mathbf{v}|}{c_s} \right\rangle, \quad (2)$$

where  $|\mathbf{v}|$  is the local magnitude of the velocity field and  $c_s$  the local sound speed, and the averaging is performed over

solid angle. We also compute the Mach number within the Si-shell and within the O-shell to characterize their behavior independently. The shell region for silicon-28 is defined as the region where  $X(^{28}\text{Si}) > 0.2$  and  $X(^{16}\text{O}) < 0.2$  and for oxygen-16  $X(^{16}\text{O}) > 0.2$  and  $X(^{28}\text{Si}) < 0.2$ .

In Figure 5 we show the time evolution of the maximum angle-averaged Mach number for all 2D models. The maximum Mach number reported at the start of the simulation reflects the initial transient as it traverses the domain. Beyond  $t \approx 15$  s, the transient has either traversed the shell region or been sufficiently damped that the Mach numbers reflect the convective properties of the shells and not the initial ra-

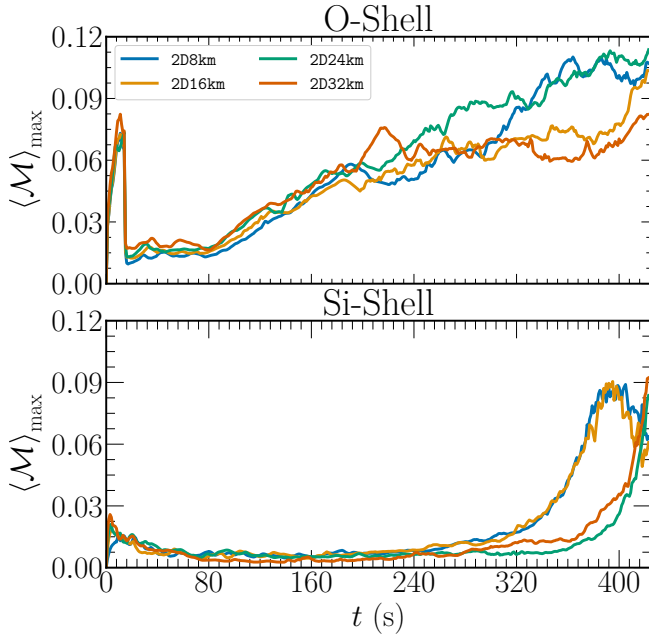


**Figure 5.** Time evolution of the maximum angle-averaged Mach number within the Si- and O-shell for all 2D models.

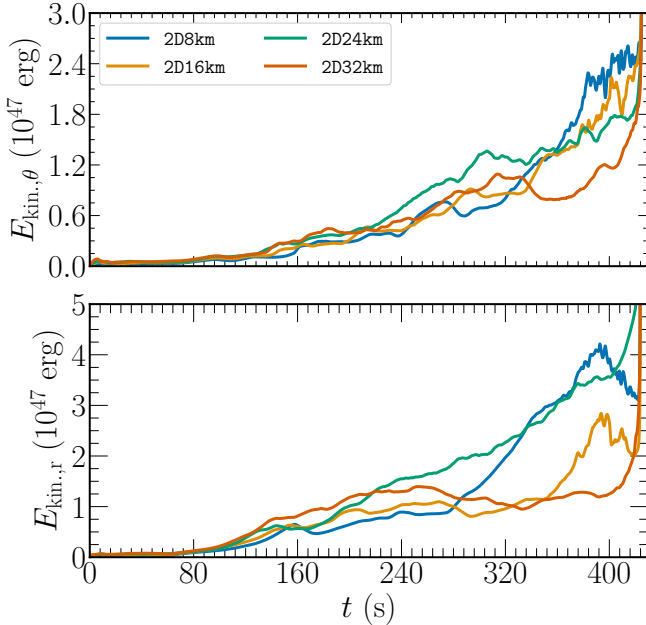


**Figure 6.** Time evolution of the radial and non-radial kinetic energy for the four 2D models.

dial wave. The Si-shell appears to reach a quasi-steady state in the first  $\approx 80$  seconds, this is seen by all models reaching a characteristic Mach number within the shell. In the O-shell, the Mach number remains relatively flat although larger than the approximate mean in the Si-shell, this suggests little to no convective activity in the O-shell during this time. To make an estimate of the time at which these two regions would be expected to reach a quasi-steady convective state,

we can estimate a convective turnover timescale for each region. The Si-shell spans a radius of approximately 800 km with convective speeds of  $v_{\text{Si-shell}} \approx 80 \text{ km s}^{-1}$  at early times. Using this, we can estimate an approximate convective turnover time within the Si-shell of  $\tau_{\text{Si}} \approx 2r_{\text{Si}}/v_{\text{Si}} \approx 20$  seconds. This value suggests that after the transient has traversed the Si-shell region, a total of approximately three turnover timescales elapse before the region reaches a quasi-steady state represented by an average Mach number oscillating on the approximate timescale of the turnover time. A similar estimate can be made to the O-shell where we determine a turnover time of  $\tau_{\text{O}} \approx 100$  seconds. This value suggests that the lack of change in Mach number for the O-shell is due to the fact that the region has not yet reached a quasi-steady convective state.

Figure 5 also shows that the time evolution of the maximum Mach number for the 2D simulations is not monotonic with resolution. While up to around 160 s the peak Mach number is consistently larger for lower resolution simulations, thereafter we find a more varied and chaotic trend. The maximum Mach number does not show a clear trend or behavior with resolution in the later parts of the simulations. We attribute this to the stochastic behavior of the turbulent convection, particularly in 2D where the role of the inverse turbulent cascade (Kraichnan 1967) and the influence of the symmetry axis can exacerbate chaotic behavior. In the highest resolution 2D model, the O-shell reaches speeds of  $v_{\text{conv.}} \approx 250 \text{ km s}^{-1}$ , slightly larger than the 16 km model. This is seen as a divergence of the two models at  $t \approx 300$  s with the more resolved model increasing in maximum Mach number value, reaching values that the 16 km model does not reach until the last  $\approx 15$  seconds prior to collapse. The 2D24km has the largest convective velocity speeds at  $t \approx 300$  s with speeds continuing to increase up to the point of collapse, this trend is reflected as the steady increase of the local maximum Mach number. The lowest resolution 2D model has convective speeds  $\approx 100 \text{ km s}^{-1}$  slower than the 2D24km at this time with speeds maintaining steady values up until the final  $\approx 20$  s before collapse, represented by the nearly constant Mach number of  $\approx 0.07$ . In the final  $\approx 20$  s, the 2D32km only slightly increases to a value of  $\approx 0.08$  at collapse. By the end of the simulation, the models span a range of Mach numbers of  $\approx 0.08 - 0.12$ .

The late time behavior of the Si-shell region of the two highest resolution models can be attributed to an expansion of the width of the convective Si-shell region observed in the last slice of Figure 4 as well as a steady increase followed by saturation of the peak mach number in Figure 5. The two highest resolution models experience a less severe initial and reflected velocity transient wave ( $\approx 20 \text{ km s}^{-1}$  larger in the 32 km model than the 8 km model), causing less deviation from hydrostatic equilibrium for the Si-shell region as

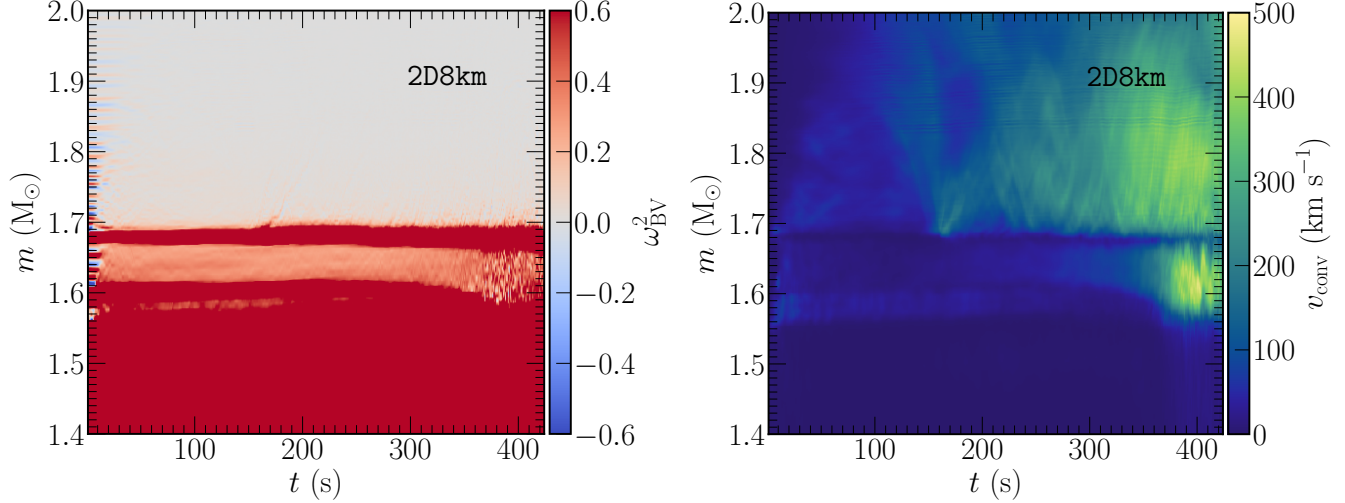


**Figure 7.** Same as in Figure 3 but for the 2D8km FLASH simulation. The slightly negative values of  $\omega_{\text{BV}}^2$  denoted by the gray/light blue regions represent regions unstable to convection.

opposed to the less resolved models. Due to less expansion in the two highest resolution models, the convective velocity speeds reach larger values in the Si-shell at earlier times, this is represented by a notable increase in the mach number from  $t \approx 300$  s to  $\approx 390$  s when a peak value or “saturation” point is reached. At this point, speeds in these models become large enough to overcome the barrier between the convective and non-convective silicon shell regions causing them to merge. After this merging of these two regions, the entire region becomes fully convective. However, due to the expansion of the width of the Si-shell region after merging, the burning within this region occurs at lower density. Because the local sound speed goes as  $c_s \propto \rho^{-1/2}$ , a decrease in density leads to an increase in the sound speed therefore decreasing the local maximum Mach number. The two lower resolution models do not experience this merging of the two regions until moments before collapse when the flow speeds are large enough  $\approx 150 \text{ km s}^{-1}$  to merge.

In Figure 6 we show the time evolution of the total kinetic energy in the radial and non-radial components for the 2D FLASH models. When considering the non-radial kinetic energy components for the four models we see that the peak value of the energy at collapse increases with an increase in model resolution with the highest resolution model showing a peak value of  $E_{\text{kin},\theta} \approx 2.5 \times 10^{47}$  erg at collapse. The radial kinetic energy shows further evidence for the expansion of the Si-shell region in the two highest resolution models with the energies showing local maxima around  $t \approx 390$  s followed by a steady decline for the duration of the simulation. This transition time is also reflected in the non-radial kinetic energy where one can notice a slight increase in the energy from  $t \approx 390$  s to collapse.

In Figure 7 (left) we show the time evolution of the Brunt-Väisälä frequency for the 2D8km model assuming the

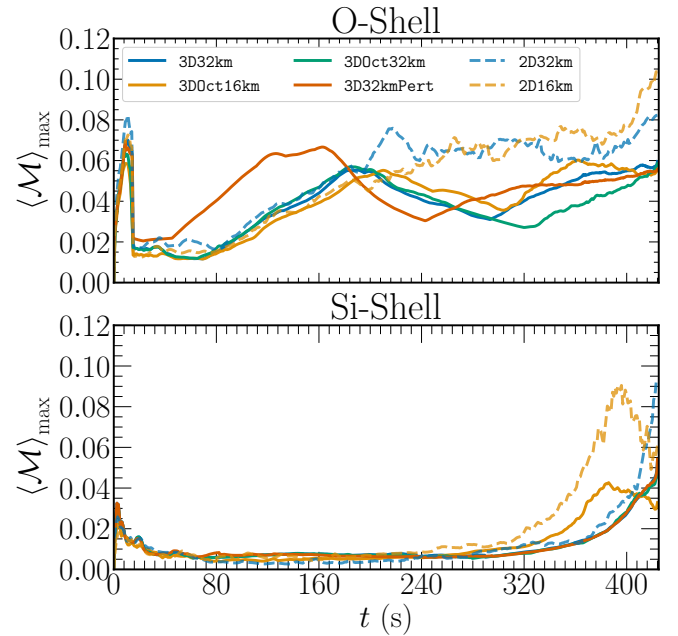


**Figure 8.** Same as in Figure 5 but for all the 3D models for the duration of the simulation. For comparison, we also plot the 2D16km and 2D32km models.

Ledoux criterion for convection which states that a region is stable against convection if

$$\nabla_{\text{rad.}} < \nabla_{\text{ad.}} - \frac{\chi_{\mu}}{\chi T} \nabla_{\mu}. \quad (3)$$

Under this criterion, we can compute the Brunt-Väisälä frequency for the FLASH simulations as

$$\omega_{\text{BV}}^2 = g \left( \frac{1}{\rho} \frac{\partial \rho}{\partial r} - \frac{1}{\rho c_s^2} \frac{\partial P}{\partial r} \right), \quad (4)$$

where  $g$  is the local gravitational acceleration,  $\rho$  the mass density,  $c_s$  the adiabatic sound speed, and  $P$  the pressure.

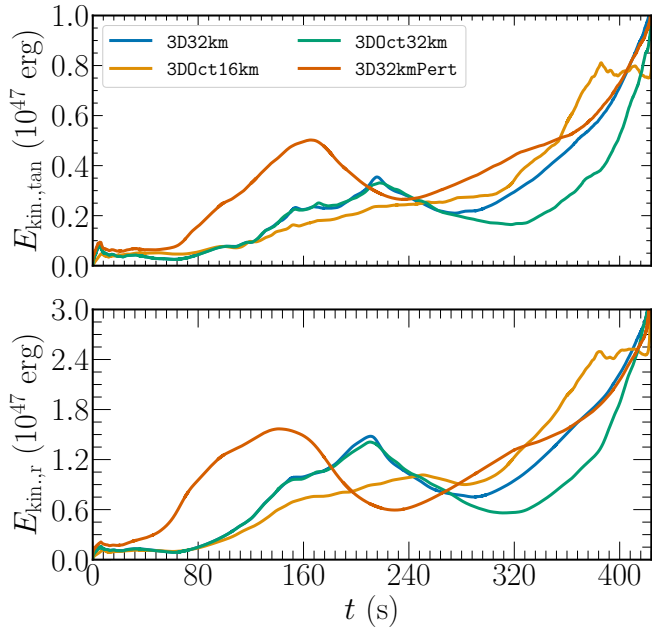


**Figure 9.** Same as in Figure 6 but for the four 3D models.

This form of the Brunt-Väisälä frequency equation is equivalent to forms that explicitly include the entropy and electron fraction gradients (Müller et al. 2016). For each timestep for which these 2D data are available, we compute angle average profiles as a function of radius before using Equation 4 to compute the frequency. Using this convention a positive value implies a region stable against convection. In multi-D simulations, the asymptotic behavior of efficient convection at evolutionary timescales will work to flatten or smooth out any entropy or composition gradients thus tending towards a Brunt-Väisälä frequency of zero. In the context of this work, we are using this quantity to identify the location of convectively active regions and compare them amongst models and to other multi-D progenitor models found in the literature (Müller et al. 2016; Jones et al. 2016; Yadav et al. 2020).

In Figure 7 we also show the time evolution of the convective velocity (right), here defined as  $v_{\text{conv}} = \sqrt{|\mathbf{v}|^2 - v_{\text{rad}}^2}$ , as a function of time for the same model. The base of the O-shell region is shown at an approximate mass coordinate of  $1.7 M_{\odot}$ . Within the O-shell, the convective velocity reach speeds of nearly  $500 \text{ km s}^{-1}$  as the model approaches iron core collapse. Prior to this, the model shows values on the order of  $50\text{-}100 \text{ km s}^{-1}$  in the Si-shell and  $200\text{-}400 \text{ km s}^{-1}$  in the O-shell. The expansion of the convective Si-shell region due to the merging is observed as well in the convective velocity, again around  $t \approx 390 \text{ s}$ , the same time at which the velocity begins to reach values observed in the O-shell for this model. In comparing to Figure 3, the FLASH model predicts two initial inner and outer convectively active regions that eventually merge into one larger region near collapse.

On the other hand, the MESA model predicts a transition of the location of the convective region followed by late time expansion of this region near collapse. Despite these somewhat different evolutionary pathways both models agree in their qualitative description of the location of the convective regions near collapse. The major difference between the two models are the magnitude of the convective velocities predicted by MESA /MLT.

### 3.2. Results from 3D Simulations

We perform a total of four 3D stellar models: two models in octant symmetry at 16 and 32 km finest grid spacing and two full  $4\pi$  models at 32 km finest resolution with and without initial perturbations. In this subsection, we will consider the global properties of all 3D models, describe the perturbed  $4\pi$  32 km in detail, and, lastly, consider the impact of octant symmetry and resolution.

In Figure 8 we show the time evolution of the maximum Mach number in the Si- and O-shell at each timestep for all 3D models. Contrary to the trend seen in Figure 5 for the O-shell one can observe a periodic nature in the Mach number values that follows our estimate for the convective turnover timescales from Section 3.1. Similar to the comparable 2D case (see Figure 6), the 3D0ct16km model appears to reach a peak Mach number in the Si-shell at around  $t \approx 390 \text{ s}$  before a steady decline as the model approaches collapse, this behavior is also attributed to expansion of the Si-shell after the merging of the convective and non-convective regions. This result suggests that the merger is independent of geometry and dimensionality but instead depends on the resolution of the inner core region.

Figure 9 shows the time evolution of the radial and non-radial kinetic energy for the four 3D models. In general, the 32 km resolution models behave similarly with the  $4\pi$  models having larger kinetic energy values than the octant model beyond  $t \approx 280 \text{ s}$ . The perturbed  $4\pi$  3D model reaches larger kinetic energy values at earlier times due to the initial injection of energy via the perturbations. The model reaches a peak in radial kinetic energy at  $t \approx 150 \text{ s}$ , roughly 70 s earlier than the unperturbed model. In terms of the total initial kinetic energy the perturbed model began with a value of  $E_{\text{kin.}} \approx 5.8 \times 10^{45} \text{ erg}$ , approximately 4% of the peak total kinetic energy observed later. The 16 km octant model has larger kinetic energy values than both models at late times while also reaching a local peak value approximately 30 s before collapse. Prior to about 200 s, the bulk of the energy in the radial direction for the two unperturbed 32 km models is due to an the initial transient that traverses the domain at the start of the simulation and leaves the domain at  $t \approx 60 \text{ s}$ . The 16 km model experiences a less significant initial transient and therefore undergoes less initial expansion/contraction as the model readjusts to a new equilibrium.

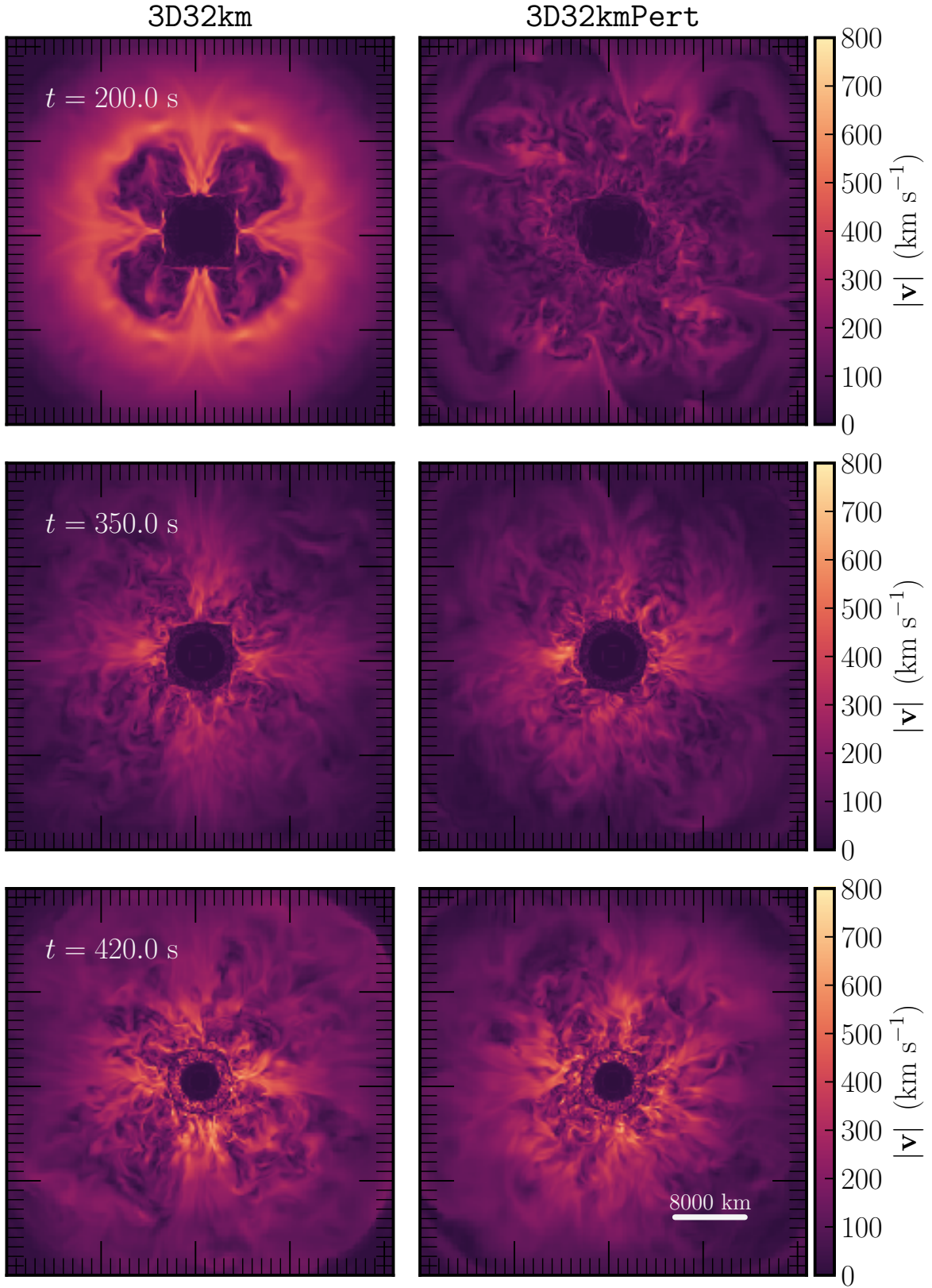


**Figure 10.** Slices of the the magnitude of the velocity field for the 3D32km (left) and 3D32kmPert (right) models at  $t = 200 \text{ s}$ ,  $350 \text{ s}$ , and  $420 \text{ s}$  in the  $x$ - $y$  plane. At a time of  $t = 200 \text{ s}$ , the unperturbed 3D32km (left) model shows a clear indication of grid scale perturbations seeded by the Cartesian grid while the perturbed model represents the imposed initial velocity field described in § 2.2. As the simulation evolves, the boxiness is lessened as the convection becomes fully developed in the 3D32km model, though still remains to some extent at the end of the simulation. At  $t = 420 \text{ s}$  (bottom panel), the qualitative structure of the O shell convection in both models is similar, though 3D32km does still show a greater impact of the Cartesian grid. Overall, both models show O-shell convection occurring at a broad range of scales with the unperturbed model having a slight preference along the Cartesian axis. The characteristic scale of the convection for both models is considered in § 3.2.1.

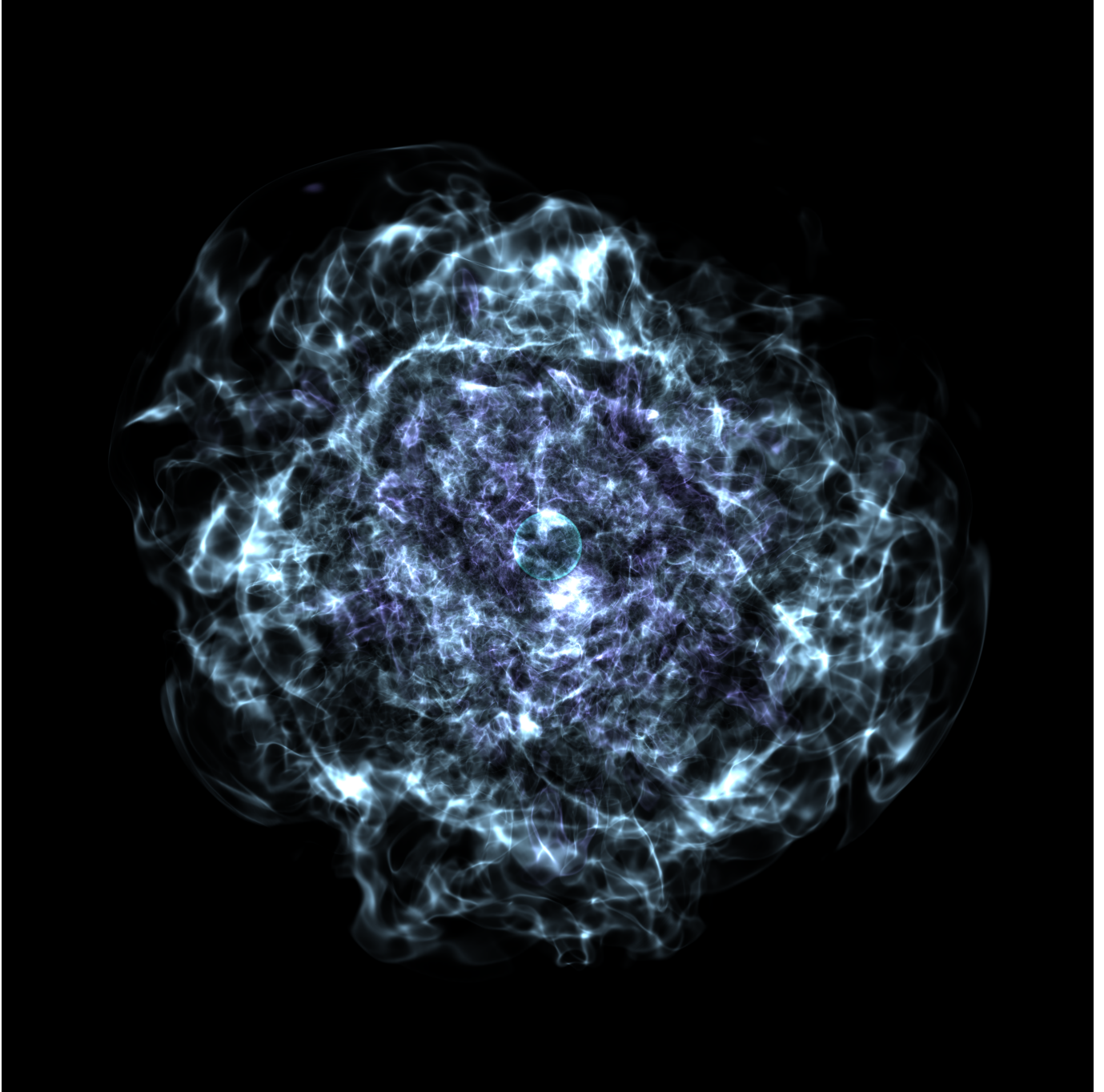


**Figure 11.** 3D volume rendering of the magnitude of the velocity field for the  $4\pi$  3D32kmPert model at a time  $\approx 2$  seconds before iron core collapse. The teal contour denotes the edge of the iron core defined to be the radius at which  $s \approx 4 k_{\text{KB}} / \text{baryon}$ . At this time, the iron core spans a radius of  $r \approx 1982$  km. The light purple plumes represent O-shell burning convection speeds following a Gaussian intensity mapping with a peak at  $|\mathbf{v}| \approx 300 \text{ km s}^{-1}$  while the light blue plumes use a similar mapping with a peak at  $|\mathbf{v}| \approx 100 \text{ km s}^{-1}$ . Both intensity mappings have a width of  $\pm 30 \text{ km s}^{-1}$  about the peak of the Gaussian curve. This image was made using `yt` and the color map library `cmocean`.

The evolution of the magnitude of the velocity field for models 3D32km (left) and 3D32kmPert (right) is compared in Figure 10. For the unperturbed case, 3D32km, convection is seeded by the Cartesian grid, resulting in a prominent boxy character to the convection in the O shell, par-

ticularly at earlier times. The boxiness is lessened as the convection becomes fully developed, though still remains to some extent at the end of the simulation. This is seen in the bottom left panel of Figure 10 as slightly larger velocities along the directions normal to the Cartesian grid. This

is to be expected since the effective numerical viscosity is larger in the diagonal directions, damping the convective velocities there. Use of high-order accurate methods, both in space and time, could alleviate this Cartesian grid effect to some extent (e.g., Rembiasz et al. 2017). For the perturbed model, 3D32kmPert, vigorous convection begins earlier, as evidenced in Figure 9, and does not show clear Cartesian grid artifacts, as can be seen in the top right panel of Figure 10. As the simulation proceeds, the influence of the Cartesian grid is still seen in 3D32kmPert to some extent resulting in slightly larger velocities along the normal directions, though still to a lesser degree than in 3D32km. Just prior to collapse (bottom panels of Figure 10), the qualitative structure of the O-shell convection in models 3D32kmPert and 3D32km is not too dissimilar, though 3D32km does still show a greater impact of the Cartesian grid. The total energy in convection is also nearly identical between the two models near collapse, as seen in Figure 9. The Si shell convection shows little to no Cartesian grid effect and is essentially identical between models 3D32kmPert and 3D32km. In Section 3.2.1 we consider properties of the convection in these two regions more quantitatively by decomposing the velocity field into spherical harmonics and comparing those results between the perturbed and non-perturbed models.

In Figure 11 we show a 3D volume rendering of the magnitude of the velocity field for the 3D32kmPert model at  $t \approx 423$  s. The approximate location of the edge of the iron core (shown in teal) is taken to be an isocontour surface at a radius where  $s \approx 4 k_{\text{KB}} / \text{baryon}$ . At this time, the iron core has a radius of  $r \approx 1982$  km. The light purple plumes show the fast moving convective motions in the O-shell region depicted by a Gaussian transfer function with a peak at  $|\mathbf{v}| \approx 300 \text{ km s}^{-1}$ . The slower moving, larger scale motions are shown using a similar transfer function with a peak at  $|\mathbf{v}| \approx 100 \text{ km s}^{-1}$  in light blue. Both intensity mappings have a width of  $\pm 30 \text{ km s}^{-1}$  about the peak of their respective Gaussian curves. The volume rendering suggests that convection is occurring in the O-shell at a broad range of convective scales.

Similar to the analysis done for the MESA model and the 2D FLASH models, in Figure 12 we show the Brunt-Väisälä frequency (left) and convective velocity (right) as a function of time for the 3D32kmPert FLASH model. Unlike the 2D8km, this model does not experience the merging of the two Si regions until a few seconds prior to collapse leading to a similar fully convective Si-shell at the end of the simulation. Another notable feature of this model is the slight expansion and then contraction of different regions of the model. For example, the base of the O-shell region begins at a mass coordinate of  $m \approx 1.68 M_{\odot}$  in all models but appears to expand outward to a coordinate of  $m \approx 1.72 M_{\odot}$  for the 3D32km model at about  $t \approx 200$  s. This expansion is not

observed in the 2D8km model but is partially due to the initial transient at the beginning of the simulation, similar to the low resolution 2D models in § 3.1. The impact of this effect on our main results will be considered in Section 3.2.2.

### 3.2.1. Characterizing the convection in the 3d32kmPert model

To characterize the scales of the convective eddies and the overall evolution of the strength of convection throughout the duration of the simulations we decompose the perturbed velocity field into spherical harmonics for both the O- and Si-shells. We compute the total power for a given spherical harmonic order,  $\ell$ , as

$$c_{\ell}^2 = \sum_{m=-\ell}^{\ell} \left| \int Y_{\ell}^m(\theta, \phi) |\mathbf{v}'| (r_{\text{shell}}, \theta, \phi) d\Omega \right|^2, \quad (5)$$

where  $|\mathbf{v}'| = |\mathbf{v}| - |\tilde{\mathbf{v}}|$ , with  $|\tilde{\mathbf{v}}|$  corresponding to the mean background flow speed at the chosen shell radius (Schaefer 2013). For the O-shell we choose to evaluate at a radius of 6000 km, while the Si-shell is evaluated at  $r = 2800$  km.

In Figure 13 we show the resulting power spectrum for the O- (left) and Si-shell (right) regions at six different times during the simulation for the 3D32kmPert model. The axis-aligned symmetry seen in the 3D32km model at  $t = 200$  s of Figure 10 is also reflected in the spectrum for the O-shell at a time of  $t = 300$  s here, where we see a peak at  $\ell = 4$  and  $\ell = 8$  indicating significant power residing in scales aligned with the Cartesian grid. At later times, the energy begins to transfer between scales with a noticeable increase in power in the  $\ell = 2$  and  $\ell = 3$  modes, while the peak of power remains at  $\ell = 4$ . In this O-shell, we also see comparable power at intermediate to small scales of  $\ell \approx 10-30$  suggesting a range of behavior for the convection. In the last  $\approx 25$  s, intermediate scales of  $\ell = 5-10$  experience an increase in power up towards the expected  $\ell^{-5/3}$  Kolmogorov scaling (dashed black line) for turbulent flows. The power spectrum for the Si-shell region follows a significantly different trend than in the O-shell region. Overall, the Si-shell region reaches a quasi-steady state at  $t \approx 300$  represented by a broad spectrum with a peak at  $\ell \approx 30-40$ . Beyond these times, the Si-shell increases in total power by  $\approx$  two orders of magnitude with the peak of the spectrum remaining constant up to the point of collapse.

This characteristic  $\ell$  for the Si-shell approximately corresponds to the aspect ratio,  $\ell \approx \pi r_{\text{shell}} / \Delta r_{\text{shell}} = 15$ , and we associate this scale with roughly the driving scale of the turbulent convection. There is only weak evidence for a significant inertial range with Kolmogorov scaling of  $\ell^{-5/3}$  in Si-shell beginning around  $\ell \approx 30$ . This is a far larger wavenumber for the start of the turbulent cascade than we see for the O-shell, which is to be expected since the Si-shell is much thinner. Similar to behavior of the spectra for the O-shell, between the driving scale and the start of Kolmogorov scaling,

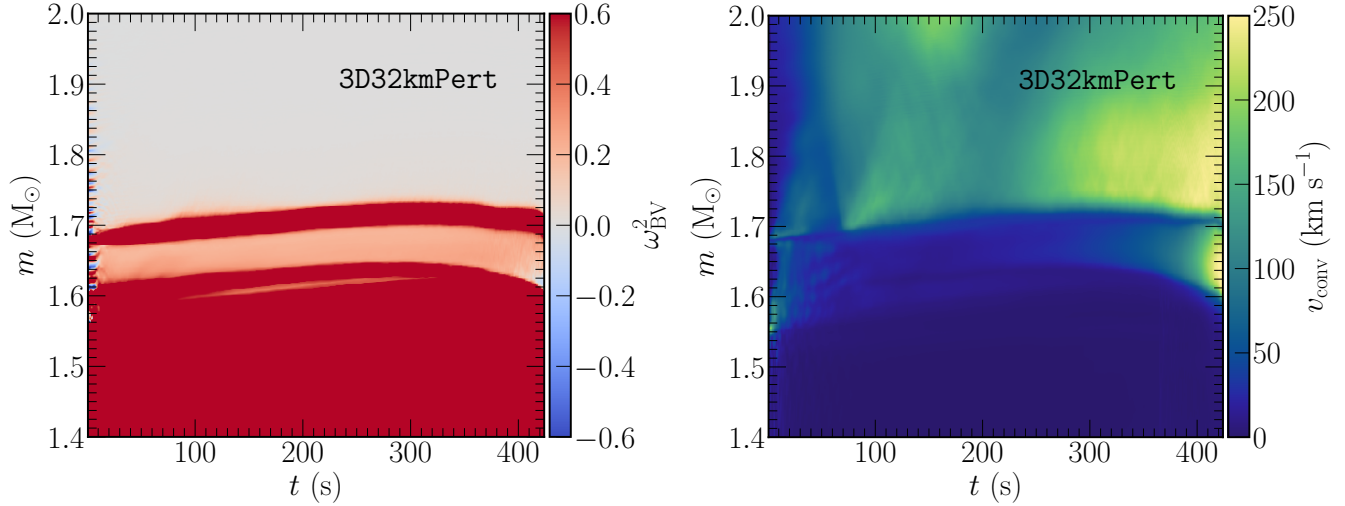


**Figure 12.** Same as in Figure 3 but for the 3D32kmPert FLASH simulation.

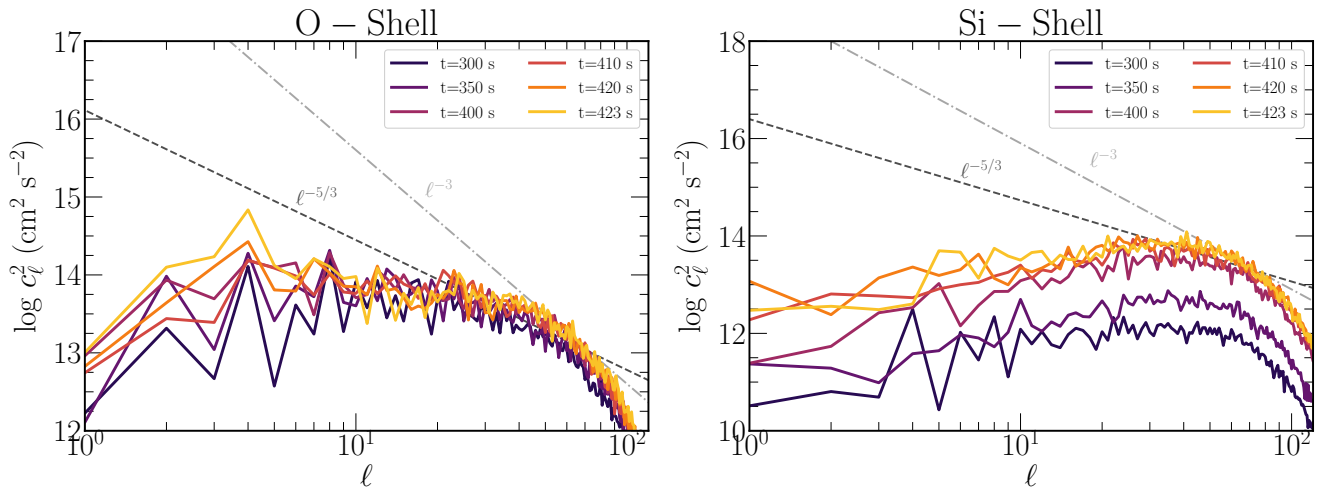


**Figure 13.** Power spectrum distribution of the spherical harmonic decomposition of the magnitude of the velocity in the O- and Si-shell regions at six different times for the 3D32kmPert model.

the spectra show behavior that is consistent with the “bottleneck” effect resulting from an inefficient cascade of turbulent energy due to insufficient resolution (Radice et al. 2015). At  $t \geq 350$  s, the power in the peak harmonic index begins to increase significantly with smaller values of  $\ell$  also experiencing an increase in power. In the last few seconds of the simulation, an increase in power for the  $\ell = 5$  mode is observed although the peak of the spectrum remains at larger  $\ell$ . At these same times, the contraction of the inner iron core is accelerating leading to an increase in the Si burning rate and, subsequently, more vigorous Si-shell convection. A similar increase in power at low  $\ell$  is also seen in the O-shell during this same period. Evidence to support this behavior is shown by the increase in Mach number within the Si-shell observed at late times in Figure 8 as well as the radial kinetic energy shown in Figure 9.

In Figure 14, we compare the power spectrum for the perturbed and non-perturbed models at  $t = 200$  s and  $t = 420$  s. At  $t = 200$  s, the unperturbed model (purple dashed line) shows an excess in power at  $\ell = 4$  and  $\ell = 8$ , also reflected by the Cartesian aligned nature of the convection shown in the top panel of Figure 10. The perturbed model (solid purple line) does not show excess power in these modes but instead shows a range of power across modes including those at larger scales at  $\ell \leq 4$ . When considering  $t = 420$  s, the spectrum of the O-shell region for the unperturbed model (dashed orange line) shows a slightly larger peak at  $\ell = 4$  and a deficit of power by an order of magnitude for the  $\ell = 2$  and  $\ell = 3$  modes. Despite these differences, the spectra at this time are relatively similar, both having a peak at  $\ell = 4$  and an intermediate range of scales just below what is expected for a Kolmogorov scaling of  $\ell^{-5/3}$ .

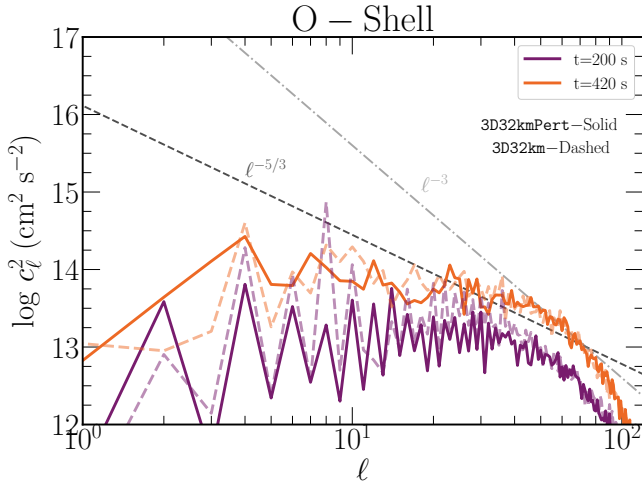


**Figure 14.** Same as in Figure 13 but only considering the O-shell region for the 3D32km and 3D32kmPert models at two different times.

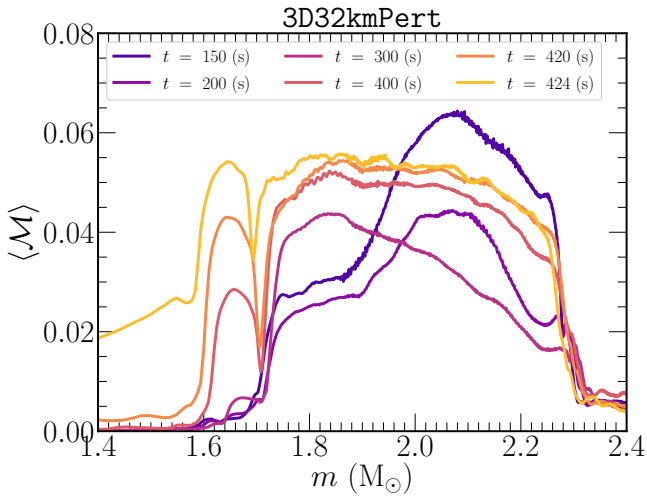


**Figure 15.** The profile of the angle averaged Mach number as a function of mass coordinate at six different times for the 3D32kmPert stellar model. At  $t = 424$  s the average Mach number reaches  $\langle \mathcal{M} \rangle \approx 0.06$  in the Si-shell and at the base of the O-shell.

In Figure 15 we show the angle-averaged Mach number profile as a function of mass coordinate for the 3D32kmPert model at six different times. The Si-shell region is situated at a mass coordinate of approximately  $1.6$  to  $1.7 M_{\odot}$ . The evolution of the Mach number in this region is further representative of the power spectra shown in Figure 13. For the majority of the simulation, the Mach numbers in this region are on the order of  $\langle \mathcal{M} \rangle \lesssim 0.01$ . Only at times beyond  $t \approx 300$  s do they increase significantly reaching values of  $\langle \mathcal{M} \rangle \approx 0.06$  prior to collapse. In the O-shell region, at mass coordinates of  $m \approx 1.7 - 2.3 M_{\odot}$ , the Mach numbers reach values of about  $\langle \mathcal{M} \rangle \approx 0.06$  as early as  $t \approx 150$ . At

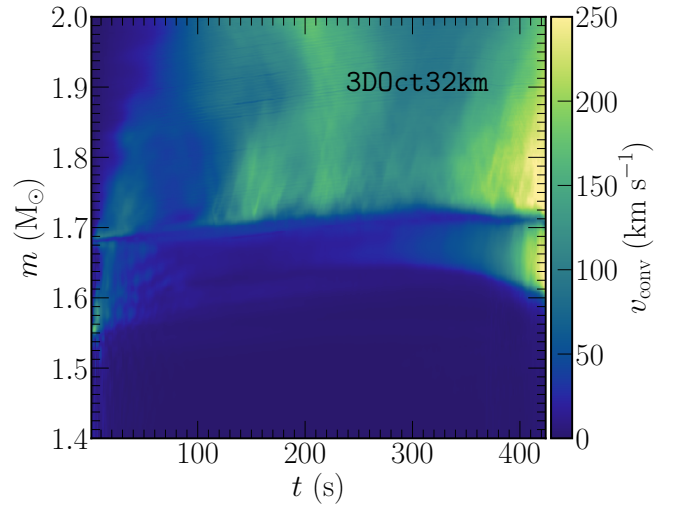
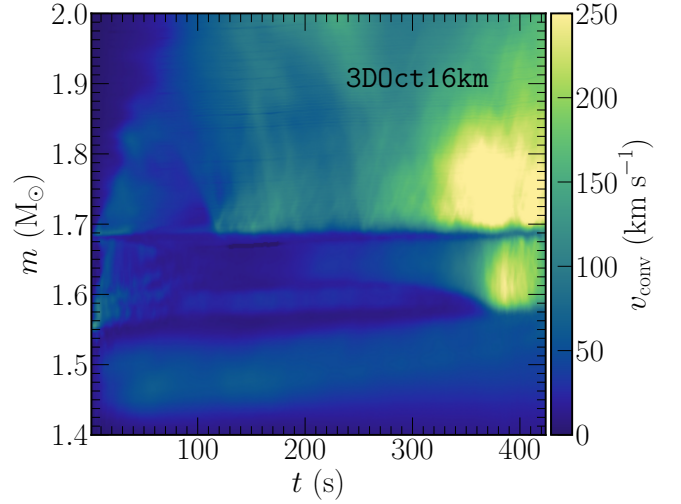


**Figure 16.** The evolution of the convection velocity profiles for the 16km and 32km 3D octant models.

late times, the O-shell region approaches Mach numbers of  $\langle \mathcal{M} \rangle \approx 0.06$  near collapse.

### 3.2.2. Effect of Spatial Resolution and Octant Symmetry

To assess the impact of spatial resolution and octant symmetry we compare the results of the two  $4\pi$  3D32km simulations with the two 3D octant models. In Figure 16 we show the time evolution of the convective velocity profiles for the 3DOct16km and 3DOct32km models. We can observe the same expansion of the O-shell region in the 32 km octant model as with the full  $4\pi$  models. In contrast, the 16 km octant model does not appear to undergo this contraction and the base of the O-shell stays at a steady mass coordinate for the duration of the simulation. Moreover, the 16 km model reaches larger convective velocities in the Si- and O-shell regions at  $t \approx 350$  s. This time corresponds to the same time at which we observe a peak in the Mach numbers

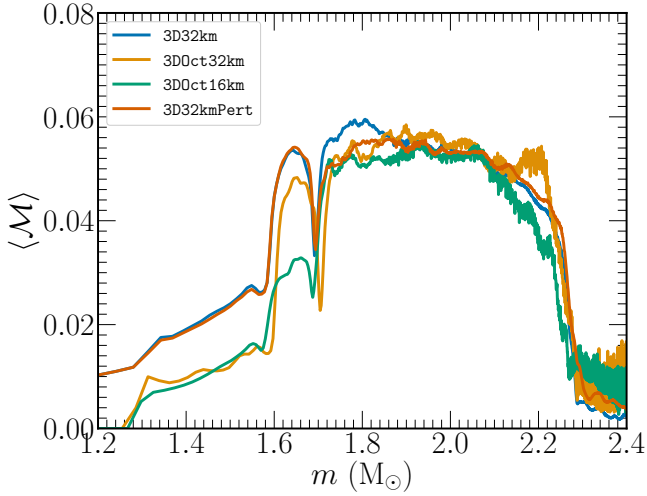


**Figure 17.** The Mach number profiles as a function of mass coordinate for the four 3D models at  $t \approx 424$  s, the start of collapse.

in Figure 8 and is due to the merging of the convective and non-convective regions. These results suggest that due to the stability of the O-shell in the 16 km model, the model follows a slightly different evolution than that of the 32 km octant and  $4\pi$  models characterized by larger convective velocity speeds that facilitate merging of convective and non-convective regions in the Si-shell. Moreover, it suggests that these differences are attributed more to the finest grid spacing of the inner core region and less dependent on the symmetry imposed for the octant models. Despite the differences found in the evolution of the Si-shell region between these two models, the O-shell region appears less impacted by the difference in resolution and arrive at similar qualitative properties among the four 3D models.

We can further determine the effect that resolution and symmetry has on our results by considering some key aspects of our 3D stellar models at collapse that have significant implications for simulations of CCSNe. Couch & Ott (2013) considered the effect of asphericities of imposed perturbations in the Si-shell regions characterized by the magnitude of the Mach number. They found large Mach number perturbations can result in enhanced strength of turbulent convection in the CCSN mechanism, aiding explosion. In Figure 17, we plot the profiles of the Mach number at the start of collapse,  $t \approx 424$  s, for the four 3D models. In general, we see that the estimates of the Mach number in the O-shell region between  $\approx 1.7$ - $2.3 M_{\odot}$  are consistent to within  $\approx 5$ – $10\%$  across all models, the largest difference observed at the base of the O-shell in the  $4\pi$  unperturbed model, showing an  $\approx 8\%$  larger value. The main difference is observed in the Si-shell region where the Mach number is approximately a factor of two larger in the 32 km models, which agree with each other to  $\approx 10\%$ .

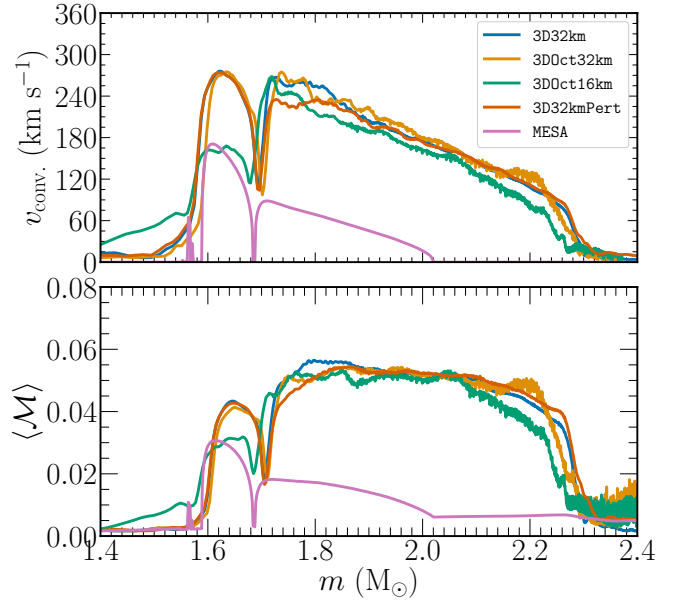


**Figure 18.** The convective velocity (top) and Mach number (bottom) for the 1D MESA model and angle-averaged profiles of the four 3D models at the  $t \approx 420$  s.

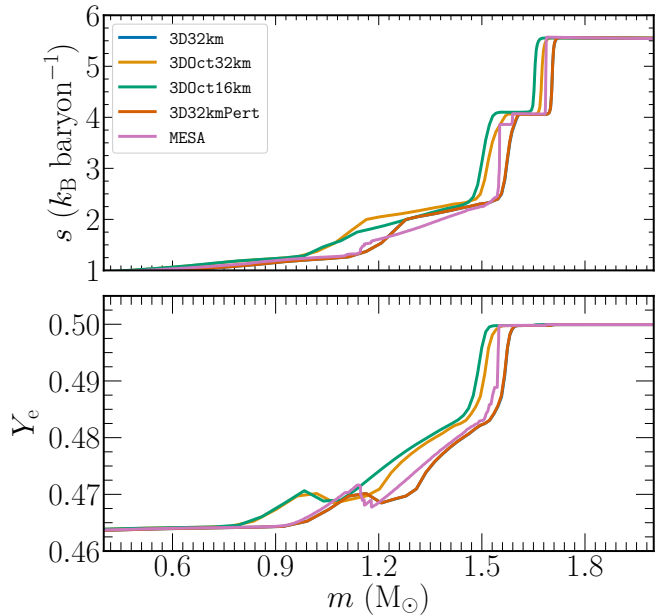


**Figure 19.** The specific entropy (top) and specific electron fraction (bottom) for the 1D MESA model and angle-averaged profiles of the four 3D models at the  $t \approx 420$  s.

Similar to the behavior seen in the two highest resolution 2D models in § 3.1, these results suggest that the expansion of the 3D models at early times due to an initial transient can affect the subsequent evolutionary properties of the Si-shell. However, the results of the O-shell are fairly robust between resolution and symmetry. The 3D0ct16km experiences a less severe initial radial transient leading to less ex-

pansion of the respective shell regions allowing the Si-shell to reach higher convective speeds at earlier times than the 32 km octant model, this is observed Figure 16. The Si-shell then reaches a “saturation” point where the shell region expands to reach a new convective stable region with a slightly larger shell that provides for slower speeds at collapse and a subsequently smaller Mach number. When comparing the 32 km octant and  $4\pi$  models it is likely the case that the convective speeds are able to reach larger values as large scale flow is not suppressed at the symmetry planes. This is supported further by the larger non-radial kinetic energy in the  $4\pi$  models as seen in Figure 9.

Another important diagnostic of the presupernova structure is the compactness parameter (O’Connor & Ott 2011),

$$\xi_m = \frac{m/M_\odot}{R(M_{\text{bary}} = m)/1000 \text{ km}} \Big|_{t=t_{\text{cc}}}, \quad (6)$$

where a value of  $2.5 M_\odot$  is typically chosen for evaluation at the start of core collapse. The value of this quantity in the progenitor star has been shown to be highly non-monotonic with ZAMS mass but gives some insight to the ensuing dynamics of the CCSN mechanism for a given progenitor (Sukhbold et al. 2018; Couch et al. 2019). We can compute this quantity for our three 3D models to determine how much variation exists due to the effects of resolution and symmetry. Using Equation (6) for the three 3D models at a time  $t = 424$  s, moments before collapse. We find values of  $\xi_{m=2.5M_\odot} = 0.0473, 0.0474, 0.0331, \text{ and } 0.0359$ , for the 3D32kmPert, 3D32km, 3DOct16km, and 3DOct32km models respectively. These values suggest that the imposed octant symmetry can under estimate the compactness of the stellar model at collapse by  $\approx 25\%$  while the differences in grid resolution but assuming octant symmetry can result in a difference of less than  $\approx 10\%$ . The compactness value at approximately the equivalent time for the MESA model was  $\xi_{m=2.5M_\odot} = 0.0492$  agreeing with the 3D32km to within less than 4%. Our values are approximately a factor of two less than those found in Sukhbold et al. (2018) and a factor of four less than those in Sukhbold & Woosley (2014) for a  $15 M_{\text{ZAMS}}$  solar metallicity progenitor. The 1D stellar evolution model presented in this work is different from those presented in Sukhbold et al. (2018) in many ways and subject to uncertainties such as input physics, mass loss rates, nuclear reactions, and resolution. Moreover, the complex interplay between various burning shells in the advanced burning stages may be chaotic in 1D leading to a stochastic behavior of measured properties for models with, for example, very slightly different initial mass (Sukhbold et al. 2018). Our 3D models provide an estimate for the variation of the compactness parameter due to different grid resolution and symmetry but should be considered in the larger context of 1D stellar

models and the other factors that can also contribute to variations in key properties.

### 3.3. Comparison between the 1- and 3D Simulations

In this subsection we compare the angle-averaged properties of the of the 1D MESA model and the four 3D models at a time near iron core collapse. In Figure 18 we show the convective velocity (top) and Mach number (bottom) for these models at  $t \approx 420$  s. Considering first the O-shell region, situated at a mass coordinate between  $m \approx 1.7 - 2.3 M_\odot$ , the convective velocity speeds of the four 3D models agree quite well in shape and magnitude. This is with exception to the 3DOct16km model for which the velocities in this region are  $\approx 5\text{-}10 \text{ km s}^{-1}$  slower. In this region, the 1D MESA model matches the shape of the convective velocity profile somewhat well but predicts a region with considerable convective activity that is smaller in extent, ranging only from  $m \approx 1.7 - 2.0 M_\odot$ . Additionally, the magnitude of the speeds in this region according to MLT are significantly less,  $\approx 4 - 5$  times less, than the values found in our 3D models. The Si-shell region is situated at a mass coordinate of  $m \approx 1.55 - 1.7 M_\odot$ . The convective speeds in the three 3D 32 km models agree well within this region while the 3DOct16km model shows a lower speed of  $v_{\text{conv.}} \approx 160 \text{ km s}^{-1}$  owing to the merging of the convectively burning and non-convectively burning regions discussed in Section 3.2. The 1D MESA model agrees with 3DOct16km remarkably well in the shape and magnitude of the convective velocity speeds in this region with only slight differences at the outer edge of the Si-shell region being steeper in the 3D model. These trends follow a similar behavior when looking at the Mach number profiles. The MESA model agrees well in shape and magnitude with the 3DOct16km model but significantly underestimates the values in the O-shell region.

We consider the core properties in Figure 19 where we show the specific entropy (top) and electron fraction (bottom) for the same models considered in Figure 18. Note that owing to the “inner boundary condition” used for the core, the specific electron fraction for all the models up to a mass coordinate of  $m \approx 0.8 M_\odot$  should be the same value. All models follow a similar specific entropy profile with only minor differences in mass of the iron core, the mass coordinate where  $s \approx 4 k_B \text{ baryon}^{-1}$ . Qualitatively, the specific entropy and electron fraction profiles for the 3D simulations are smoother than those of the MESA model.

## 4. SUMMARY AND DISCUSSION

We have investigated the long term, multidimensional, hydrodynamical evolution of a  $15 M_\odot$  star for the final seven minutes of Si- and O- shell burning prior to and up to the point of iron core collapse. Using the FLASH simulation framework we evolved eight stellar models at varying resolution, dimensions, and symmetries to characterize the nature

of the convective properties of the stellar models and their implications for CCSN explosions.

We find that in general many of the angle averaged properties of the multidimensional models were consistent with predictions made by MESA. The largest differences observed were found when comparing the convective velocities in the O-shell region to those in the MESA model. In this region, the 3D models shows convective velocity speeds that were 4-5 times larger and maximum Mach numbers that were approximately a factor of three more than as predicted by MESA. This large difference can have quantitative implications for the CCSN mechanism. Specifically, the larger velocities which can reduce the needed effective heating behind the stalled shock by instead increasing the total stress behind the shock (Murphy et al. 2013; Couch & Ott 2013, 2015; Muller & Janka 2015). For instance, Couch & Ott (2015) find that a perturbed 3D progenitor model reduced the need for increased neutrino heating to achieve successful explosion. Our 2D models showed a convectively active Si-shell region with peak velocities of approximately  $500 \text{ km s}^{-1}$  near collapse and Mach numbers of  $\approx 0.1$  near collapse. Within the O-shell region the 2D models show slightly slower convective speeds of  $\approx 400 \text{ km s}^{-1}$  and Mach numbers of 0.8-0.12 depending on the resolution of the simulation. The 3D models show velocities and Mach numbers lower than this in all cases. The  $4\pi$  3D models had convective velocities of  $\approx 240\text{-}260 \text{ km s}^{-1}$  in the Si- and O- shell moments prior to collapse with Mach values of 0.06. However, in our highest resolution 3D model (3DOct16km), the Si-shell region reached a lower convective Mach number of  $\approx 0.03$ . Our 3D models suggest Si-shell peak Mach numbers of 0.03-0.06 while the O-shell values are consistent across all models to  $\approx 5\text{-}10\%$  at  $\langle \mathcal{M} \rangle \approx 0.06$ .

To characterize the behavior of the convection of the  $4\pi$  3D models, we computed power spectra of the Si- and O-shell regions by decomposing the velocity field into spherical harmonics at different times throughout the simulation. The spectra computed for the O-shell region showed a peak at  $\ell = 4$  with non-negligible power at even larger scales near collapse. In this region, comparable power was found at intermediate to small scales of  $\ell \approx 10\text{-}30$  despite the bulk of power being stored at large scales of  $\ell \approx 2\text{-}4$  near collapse. The Si-shell region showed a rather broad spectrum at early times with a peak at  $\ell \approx 30\text{-}40$ . In the final  $\approx$  seconds of the simulation, we found the spectrum increased significantly in power with the peak of the spectrum remaining at  $\ell \approx 30\text{-}40$  but showing an increase in power at  $\ell \approx 5$ .

We also consider the impact of grid resolution on our results. We find that our highest resolution 2D (8 km and 16 km) and 3DOct16km models showed different behavior in the Si-shell than the other, less resolved models. This behavior is attributed to a less severe initial and reflected transient

in these higher resolution models allowing them to maintain better hydrostatic equilibrium (undergo less shell expansion). The subsequent result was a Si-shell region that reached higher convective velocities at earlier times than that of their lower resolution 3D counterparts leading to the merging of convective and non-convective regions in the Si-shell. The end result was a wider Si-shell region that gave Mach numbers a factor of two smaller than in the higher resolution models. The results were found to be independent of the dimensionality as they occurred in the 16 km 3D octant and 2D high resolution models. However, despite the differences between these evolutionary paths in the Si-shell, the results of the O-shell region appear largely unaffected by resolution or geometry, resulting in quantitatively similar properties near collapse in all of the 3D models. When comparing the four 3D models for different resolutions and symmetries we also found that the Mach number profiles in the O-shell region agreed across all models with only a slight difference shown in the  $4\pi$  unperturbed model where larger Mach numbers ( $\approx 8\%$ ) are found at the base of the O-shell. The Si-shell region Mach number profiles showed that the 3DOct16km model has a smaller value of  $\approx 0.03$  while the 3DOct32km reached a value approximately twice of that. This difference is again linked to the merging of the convective and non-convective regions in the 16 km models. Another important diagnostic linking the presupernova structure to the dynamics of the CCSN mechanism is the compactness parameter. When comparing values of this parameter, we find that the  $4\pi$  3D models agreed with the value computed for the 1D MESA model at collapse to within  $\sim 4\%$ . However, we show that differences in resolution for the 3D models can lead to a  $\sim 25\%$  variation while the assumed octant symmetry could lead to a  $\sim 10\%$  variation. The magnitude of these variations suggest that they can be on order of the variations found due to varying spatial resolution (Sukhbold et al. 2018), size of nuclear reaction network (Farmer et al. 2016), and nuclear reaction rate uncertainties of 1D pre-supernova models (Fields et al. 2018).

In C15, they investigated the final three minutes of Si-shell burning in a  $15M_{\odot}$  star evolved assuming octant symmetry and a reaction network that included enhanced electron capture rates. They found that convective speeds in the silicon shell reach values of  $80\text{-}140 \text{ km s}^{-1}$  near collapse. These values are approximately a factor of two-three smaller than what we find in all of our 3D simulations and a factor of four smaller than the results suggested by our 2D models. A major cause of these differences can likely be attributed to the length of their simulation. In all our multidimensional models considered here the convective velocity speeds did not increase considerably until about five minutes into the simulation. Measuring the turbulent kinetic energy power spectrum for their model they found the bulk of the energy residing at

small  $l$  values (large scales), at  $l \approx 4$  due to the imposed octant symmetry. They also found significant power at an  $l \approx 10$  value for the Si-shell region near collapse. This is a larger scale than observed in our  $4\pi$  3D perturbed model where we observe a peak in the Si-shell spectrum at  $l = 30-40$  in the final 20 seconds prior to collapse.

Müller et al. (2016) investigated the last minutes of O-shell burning in a  $18 M_{\odot}$  star. They evolved the model for  $\approx$  five minutes using a contracting inner boundary condition situated at the base of the O-shell mapped to follow the mass trajectory from the initial `Kepler` model. In their simulation of O-shell burning they find transverse velocity speeds that reach values of  $\approx 250 \text{ km s}^{-1}$  approximately a minute prior to collapse. These values are slightly larger by about  $50-100 \text{ km s}^{-1}$  than the values we find in all of our 3D models at a similar epoch. At the onset of collapse, they observe peak Mach numbers in the O-shell of  $\langle \mathcal{M} \rangle \approx 0.1$  where we find a value of  $\sim 0.06$ . They compute the power spectrum for the radial velocity component into spherical harmonics to characterize the scale of the convection. At the early times,  $t = 90.9 \text{ s}$  they find a similar characteristic scale at  $l \approx 4$  where the bulk of the power resides. As the simulation evolves the bulk of the power in their model shifts to larger scales at  $l \approx 2-4$ . Near the onset of collapse Müller et al. (2016) observe the emergence of a large scale mode at  $l \approx 2$ . In our simulation, we see a significant increase in power at  $l = 2$  and  $l = 3$  but our peak in the distribution resides at  $l = 4$ .

Recently, Yadav et al. (2020) presented a  $4\pi$  3D simulation of O-/Ne-shell burning using a similar method as presented in Müller et al. (2016). The simulation was evolved for 420 s and captured the merging of a large scale O-Ne shell merger leading to significant deviations from the properties predicted by the 1D initial model. In this work, they found at  $t \approx 250 \text{ s}$ , the barrier separating the O- and Ne-shells disappears due to an increase in entropy in the O-shell leading to the merging of the two convective regions. The merger leads to large scale density fluctuations characterized by  $l \approx 1-2$  modes within the merged shell. After the merger they observe velocity fluctuations on the order of  $800 \text{ km s}^{-1}$  that increase to as large as  $1600 \text{ km s}^{-1}$  near collapse. At collapse they observe Mach numbers of  $\approx 0.13$  in the O/Ne mixed region. These values both suggest that the merger can lead to significantly larger deviations from spherical symmetry than as suggested by the model presented in this work and other simulations of quasi-steady state convection prior to core collapse. Despite the merging of the two unique convective regions in the Si-shell observed in most of our models, we do not observe merging of different burning shell regions in any of our models.

High resolution, long term,  $4\pi$  3D simulations of CCSN progenitors can provide accurate initial conditions for simulations of CCSNe. An accurate representation of the state of the progenitor prior to collapse can have a favorable impact on the delayed neutrino-driven explosion mechanism and has important implications for the predictions of key observables from CCSN simulations. In addition to fully 3D convection motions, most massive stars are also rotating differentially in their cores. In the presence of weak seed magnetic fields, this rotation can facilitate a large scale dynamo that can have an impact on the progenitor evolution and the explosion mechanism. As such, a next step in increasing the physics fidelity of supernova progenitor models would be to consider the impact of a rotating and magnetic progenitor on the observed scale and magnitude of perturbations within the late time burning shell regions. The direct link between multidimensional rotating and magnetic CCSN progenitors and the CCSN mechanism is an important question and is the direction of future work.

*Software:* MESA (Paxton et al. 2011, 2013, 2015, 2018, <http://mesa.sourceforge.net>), MESA (Fryxell et al. 2000, <http://flash.uchicago.edu/site/>), yt (Turk et al. 2011, <https://yt-project.org>), and matplotlib (Hunter 2007, <https://matplotlib.org>), SHTns (Schaeffer 2013).

## ACKNOWLEDGMENTS

We thank S. Jones, P. Grete, J. Ranta, P. N. Sagan, and M. Zingale for useful discussions. We thank the anonymous referee for helping significantly improve a previous version of this manuscript. C.E.F. acknowledges support from a Predoctoral Fellowship administered by the National Academies of Sciences, Engineering, and Medicine on behalf of the Ford Foundation, an Edward J Petry Graduate Fellowship from Michigan State University, and the National Science Foundation Graduate Research Fellowship Program under grant number DGE1424871. SMC is supported by the U.S. Department of Energy, Office of Science, Office of Nuclear Physics, under Award Numbers DE-SC0015904 and DE-SC0017955. This work was supported in part by Michigan State University through computational resources provided by the Institute for Cyber-Enabled Research. This research made extensive use of the SAO/NASA Astrophysics Data System (ADS).

## REFERENCES

- Arnett, D. 1994, *ApJ*, 427, 932, doi: [10.1086/174199](https://doi.org/10.1086/174199)
- Arnett, D., Meakin, C., & Young, P. A. 2009, *ApJ*, 690, 1715. <https://arxiv.org/abs/0809.1625>

- Arnett, W. D., & Meakin, C. 2011, *ApJ*, 733, 78, doi: [10.1088/0004-637X/733/2/78](https://doi.org/10.1088/0004-637X/733/2/78)
- Böhm-Vitense, E. 1958, *ZA*, 46, 108
- Botticella, M. T., Smartt, S. J., Kennicutt, R. C., et al. 2012, *A&A*, 537, A132, doi: [10.1051/0004-6361/201117343](https://doi.org/10.1051/0004-6361/201117343)
- Côté, B., O'Shea, B. W., Ritter, C., Herwig, F., & Venn, K. A. 2017, *ApJ*, 835, 128, doi: [10.3847/1538-4357/835/2/128](https://doi.org/10.3847/1538-4357/835/2/128)
- Couch, S. M., Chatzopoulos, E., Arnett, W. D., & Timmes, F. X. 2015, *ApJL*, 808, L21, doi: [10.1088/2041-8205/808/1/L21](https://doi.org/10.1088/2041-8205/808/1/L21)
- Couch, S. M., Graziani, C., & Flocke, N. 2013, *ApJ*, 778, 181, doi: [10.1088/0004-637X/778/2/181](https://doi.org/10.1088/0004-637X/778/2/181)
- Couch, S. M., & O'Connor, E. P. 2014, *ApJ*, 785, 123, doi: [10.1088/0004-637X/785/2/123](https://doi.org/10.1088/0004-637X/785/2/123)
- Couch, S. M., & Ott, C. D. 2013, *ApJL*, 778, L7, doi: [10.1088/2041-8205/778/1/L7](https://doi.org/10.1088/2041-8205/778/1/L7)
- . 2015, *ApJ*, 799, 5, doi: [10.1088/0004-637X/799/1/5](https://doi.org/10.1088/0004-637X/799/1/5)
- Couch, S. M., Warren, M. L., & O'Connor, E. P. 2019, arXiv e-prints, arXiv:1902.01340. <https://arxiv.org/abs/1902.01340>
- Cox, J. P., & Giuli, R. T. 1968, *Principles of Stellar Structure* (New York: Gordon & Breach)
- Dubey, A., Antypas, K., Ganapathy, M. K., et al. 2009, *Parallel Computing*, 35, 512, doi: <https://doi.org/10.1016/j.parco.2009.08.001>
- Farmer, R., Fields, C. E., Petermann, I., et al. 2016, *ApJS*, 227, 22, doi: [10.3847/1538-4365/227/2/22](https://doi.org/10.3847/1538-4365/227/2/22)
- Farmer, R., Fields, C. E., & Timmes, F. X. 2015, *ApJ*, 807, 184, doi: [10.1088/0004-637X/807/2/184](https://doi.org/10.1088/0004-637X/807/2/184)
- Fields, C. E., Timmes, F. X., Farmer, R., et al. 2018, *ApJS*, 234, 19, doi: [10.3847/1538-4365/aaa29b](https://doi.org/10.3847/1538-4365/aaa29b)
- Fryxell, B., Olson, K., Ricker, P., et al. 2000, *ApJS*, 131, 273, doi: [10.1086/317361](https://doi.org/10.1086/317361)
- Glas, R., Just, O., Janka, H. T., & Obergaulinger, M. 2019, *ApJ*, 873, 45
- Hanke, F., Müller, B., Wongwathanarat, A., Marek, A., & Janka, H.-T. 2013, *ApJ*, 770, 66
- Heger, A., Langer, N., & Woosley, S. E. 2000, *ApJ*, 528, 368
- Heger, A., & Woosley, S. E. 2010, *ApJ*, 724, 341, doi: [10.1088/0004-637X/724/1/341](https://doi.org/10.1088/0004-637X/724/1/341)
- Hopkins, P. F., Quataert, E., & Murray, N. 2011, *MNRAS*, 417, 950, doi: [10.1111/j.1365-2966.2011.19306.x](https://doi.org/10.1111/j.1365-2966.2011.19306.x)
- Hunter, J. D. 2007, *Computing In Science & Engineering*, 9, 90
- Janka, H.-T. 2012, *Annual Review of Nuclear and Particle Science*, 62, 407, doi: [10.1146/annurev-nucl-102711-094901](https://doi.org/10.1146/annurev-nucl-102711-094901)
- Jones, S., Andrassy, R., Sandalski, S., et al. 2016, arXiv e-prints. <https://arxiv.org/abs/1605.03766>
- Kraichnan, R. H. 1967, *Physics of Fluids*, 10, 1417
- Lai, D., & Goldreich, P. 2000, *ApJ*, 535, 402
- Langanke, K., & Martínez-Pinedo, G. 2000, *Nuclear Physics A*, 673, 481, doi: [10.1016/S0375-9474\(00\)00131-7](https://doi.org/10.1016/S0375-9474(00)00131-7)
- Lee, D., & Deane, A. E. 2009, *Journal of Computational Physics*, 228, 952, doi: <https://doi.org/10.1016/j.jcp.2008.08.026>
- Lentz, E. J., Bruenn, S. W., Hix, W. R., et al. 2015, *ApJL*, 807, L31
- Mabanta, Q. A., & Murphy, J. W. 2018, *ApJ*, 856, 22, doi: [10.3847/1538-4357/aaec7](https://doi.org/10.3847/1538-4357/aaec7)
- Mazurek, T. J., Truran, J. W., & Cameron, A. G. W. 1974, *Ap&SS*, 27, 261, doi: [10.1007/BF00643877](https://doi.org/10.1007/BF00643877)
- Meakin, C. A., & Arnett, D. 2007, *ApJ*, 665, 690, doi: [10.1086/519372](https://doi.org/10.1086/519372)
- Muller, B., & Janka, H.-T. 2015, *Monthly Notices of the Royal Astronomical Society*, 448, 2141, doi: [10.1093/mnras/stv101](https://doi.org/10.1093/mnras/stv101)
- Müller, B., Melson, T., Heger, A., & Janka, H.-T. 2017, *MNRAS*, 472, 491
- Müller, B., Viallet, M., Heger, A., & Janka, H.-T. 2016, arXiv e-prints. <https://arxiv.org/abs/1605.01393>
- Murphy, J. W., Dolence, J. C., & Burrows, A. 2013, *ApJ*, 771, 52
- Nagakura, H., Burrows, A., Radice, D., & Vartanyan, D. 2019, arXiv e-prints. <https://arxiv.org/abs/1905.03786>
- O'Connor, E., & Ott, C. D. 2011, *ApJ*, 730, 70, doi: [10.1088/0004-637X/730/2/70](https://doi.org/10.1088/0004-637X/730/2/70)
- O'Connor, E. P., & Couch, S. M. 2018a, *ApJ*, 865, 81, doi: [10.3847/1538-4357/aadcf7](https://doi.org/10.3847/1538-4357/aadcf7)
- . 2018b, *ApJ*, 854, 63, doi: [10.3847/1538-4357/aaa893](https://doi.org/10.3847/1538-4357/aaa893)
- Özel, F., Psaltis, D., Narayan, R., & Santos Villarreal, A. 2012, *ApJ*, 757, 55, doi: [10.1088/0004-637X/757/1/55](https://doi.org/10.1088/0004-637X/757/1/55)
- Paxton, B., Bildsten, L., Dotter, A., et al. 2011, *ApJS*, 192, 3, doi: [10.1088/0067-0049/192/1/3](https://doi.org/10.1088/0067-0049/192/1/3)
- Paxton, B., Cantiello, M., Arras, P., et al. 2013, *ApJS*, 208, 4, doi: [10.1088/0067-0049/208/1/4](https://doi.org/10.1088/0067-0049/208/1/4)
- Paxton, B., Marchant, P., Schwab, J., et al. 2015, *ApJS*, 220, 15, doi: [10.1088/0067-0049/220/1/15](https://doi.org/10.1088/0067-0049/220/1/15)
- Paxton, B., Schwab, J., Bauer, E. B., et al. 2018, *ApJS*, 234, 34, doi: [10.3847/1538-4365/aaa5a8](https://doi.org/10.3847/1538-4365/aaa5a8)
- Paxton, B., Smolec, R., Gaudy, A., et al. 2019, arXiv e-prints. <https://arxiv.org/abs/1903.01426>
- Pignatari, M., Herwig, F., Hirschi, R., et al. 2016, *ApJS*, 225, 24, doi: [10.3847/0067-0049/225/2/24](https://doi.org/10.3847/0067-0049/225/2/24)
- Radice, D., Couch, S. M., & Ott, C. D. 2015, *Computational Astrophysics and Cosmology*, 2, 7
- Radice, D., Ott, C. D., Abdikamalov, E., et al. 2016, *ApJ*, 820, 76
- Rembiasz, T., Obergaulinger, M., Cerdá-Durán, P., Aloy, M.-Á., & Müller, E. 2017, *ApJS*, 230, 18
- Roberts, L. F., Ott, C. D., Haas, R., et al. 2016, *ApJ*, 831, 98, doi: [10.3847/0004-637X/831/1/98](https://doi.org/10.3847/0004-637X/831/1/98)
- Schaeffer, N. 2013, *Geochemistry, Geophysics, Geosystems*, 14, 751, doi: [10.1002/ggge.20071](https://doi.org/10.1002/ggge.20071)
- Su, K.-Y., Hopkins, P. F., Hayward, C. C., et al. 2018, *MNRAS*, 480, 1666, doi: [10.1093/mnras/sty1928](https://doi.org/10.1093/mnras/sty1928)
- Sukhbold, T., Ertl, T., Woosley, S. E., Brown, J. M., & Janka, H.-T. 2016, *ApJ*, 821, 38, doi: [10.3847/0004-637X/821/1/38](https://doi.org/10.3847/0004-637X/821/1/38)

- Sukhbold, T., & Woosley, S. E. 2014, *ApJ*, 783, 10,  
doi: [10.1088/0004-637X/783/1/10](https://doi.org/10.1088/0004-637X/783/1/10)
- Sukhbold, T., Woosley, S. E., & Heger, A. 2018, *ApJ*, 860, 93,  
doi: [10.3847/1538-4357/aac2da](https://doi.org/10.3847/1538-4357/aac2da)
- Timmes, F. X., Hoffman, R. D., & Woosley, S. E. 2000, *ApJS*, 129,  
377
- Timmes, F. X., & Swesty, F. D. 2000, *ApJS*, 126, 501
- Timmes, F. X., Woosley, S. E., & Weaver, T. A. 1995, *ApJS*, 98,  
617
- Toro, E. F. 1999, *Riemann Solvers and Numerical Methods for  
Fluid Dynamics* (Springer, Berlin, Heidelberg)
- Trampedach, R., Stein, R. F., Christensen-Dalsgaard, J., Nordlund,  
Å., & Asplund, M. 2014, *MNRAS*, 445, 4366,  
doi: [10.1093/mnras/stu2084](https://doi.org/10.1093/mnras/stu2084)
- Turk, M. J., Smith, B. D., Oishi, J. S., et al. 2011, *ApJS*, 192, 9,  
doi: [10.1088/0067-0049/192/1/9](https://doi.org/10.1088/0067-0049/192/1/9)
- Vartanyan, D., Burrows, A., Radice, D., Skinner, M. A., &  
Dolence, J. 2019, *MNRAS*, 482, 351
- Viallet, M., Meakin, C., Arnett, D., & Mocák, M. 2013, *ApJ*, 769,  
1, doi: [10.1088/0004-637X/769/1/1](https://doi.org/10.1088/0004-637X/769/1/1)
- Woosley, S. E., & Heger, A. 2007, *PhR*, 442, 269,  
doi: [10.1016/j.physrep.2007.02.009](https://doi.org/10.1016/j.physrep.2007.02.009)
- . 2015, *ApJ*, 810, 34, doi: [10.1088/0004-637X/810/1/34](https://doi.org/10.1088/0004-637X/810/1/34)
- Woosley, S. E., Heger, A., & Weaver, T. A. 2002, *Rev. Mod. Phys.*,  
74, 1015, doi: [10.1103/RevModPhys.74.1015](https://doi.org/10.1103/RevModPhys.74.1015)
- Yadav, N., Müller, B., Janka, H. T., Melson, T., & Heger, A. 2020,  
*ApJ*, 890, 94, doi: [10.3847/1538-4357/ab66bb](https://doi.org/10.3847/1538-4357/ab66bb)
- Zingale, M., Dursi, L. J., ZuHone, J., et al. 2002, *ApJS*, 143, 539,  
doi: [10.1086/342754](https://doi.org/10.1086/342754)